공학석사 학위논문

Interfacial Modification and Novel Nanocomposite Design for Efficient and Stable CuSCN-Based Perovskite Solar Cells

계면 조정 및 새로운 나노 복합체 디자인을 통한 고효율, 고안정성의 CuSCN 기반 페로브스카이트 태양전지

2020년 8월

서울대학교 대학원
재료공학부
이 영 현

Abstract

Organic–inorganic hybrid perovskite solar cells (PSCs) are considered as one of the most promising emerging photovoltaics with outstanding performance. However, the commonly used organic hole transport materials (HTMs) suffer from heat-, light-, and bias-induced degradation along with defect diffusion and hygroscopic properties. To resolve these issues in conventional HTMs, inorganic materials with superior chemical stability, high carrier mobility, and low cost have been developed, demonstrating improved stability under rigorous conditions such as high temperature and long-term illumination. Understanding the properties of alternative inorganic HTMs is of prominent importance to realize more stable and efficient PSCs. The study of the inorganic hole-transport layer (HTL) in perovskite solar cells (PSCs) is gathering attention because of the drawback of the conventional PSC design, where the organic HTL with salt dopants majorly participates in the degradation mechanisms. On the other hand, inorganic HTL secures better stability, while it offers difficulties in the deposition and interfacial control to realize high performing devices. To prevent the degradation, inorganic-based CuSCN HTL emerged as an alternative, yet the interfacial reactivity is not clearly elucidated.

Polydimethylsiloxane (PDMS) was demonstrated as an ideal polymeric interlayer which prevents interfacial degradation and improves both photovoltaic performance and stability of CuSCN-based PSC by its cross-linking behavior. Surprisingly, the PDMS polymers are identified to form chemical bonds with perovskite and CuSCN, as shown by Raman spectroscopy. This novel cross-linking

interlayer of PDMS enhances the hole-transporting property at the interface and passivates the interfacial defects, realizing the PSC with high power-conversion efficiency over 19%. Furthermore, the utilization of the PDMS interlayer greatly improves the stability of solar cells against both humidity and heat by mitigating the interfacial defects and interdiffusion. The PDMS-interlayered PSCs retained over 90% of the initial efficiencies, both after 1000 h under ambient conditions (unencapsulated) and after 500 h under 85°C/85% relative humidity (encapsulated).

Cu_2O and CuSCN are co-utilized as efficient and stable hole-transporting layer. Cu_2O is known for the material that has the highest hole mobility, but the formation of uniform film remained as main difficulty due to the limited selection of solvent and poor film formation. Therefore, Cu_2O-CuSCN nanocomposite excellently fabricated as an idea HTL, exhibiting 19.2% of power conversion efficiency (PCE) and sustaining its efficiency for 720 h under extreme condition (85°C/85% of relative humidity, encapsulated). Chemical distribution of nanocomposite HTL was analyzed by secondary-ion spectroscopy (SIMS), elucidating Cu_2O is clearly protecting the interface between the perovskite and CuSCN to reduce the interfacial reaction. Also, the excellent hole transporting property of Cu_2O improved the charge extraction rate and reduced recombination, which were conducted by photoluminescence (PL) and electrochemical impedance spectroscopy (EIS).

Keywords : perovskite solar cells, inorganic hole-transport layer, defect control, cross-linking interlayer, nanocomposite, stability.

Student Number : 2018-24358

Table of Contents

List of Figures

Chapter 1.

Chapter 2.

Sheet resistance is measured by four-point probe for CuSCN and PDMS/CuSCN films, which are deposited on (a) quartz substrates and (b) $MAPbI_3$ films.

Fig. 2-6. (Color) Space-charge limited current (SCLC) measured for CuSCN and PDMS/CuSCN films. (a) *J-V* characteristics of hole-only devices without perovskite layer, measured in dark condition. (b) $J^{0.5}$-V plot in the SCLC region with high applied voltage. The hole mobilities μ_h are calculated to be 0.20 and 0.18 cm^2 V^{-1} s^{-1}, for CuSCN and PDMS/CuSCN films respectively.

Fig. 2-7. (Color) Ultraviolet photoemission spectroscopy measurement for various surfaces. Photoemission spectra for (a) secondary electron edge and (b) valence band edge on the surfaces of CuSCN HTLs with and without PDMS interlayer.

Fig. 2-8. (Color) Passivation of defects by the PDMS interlayer. (a) Nyquist plots and (b) trap distribution spectra of the $MAPbI_3$/CuSCN-based PSCs with and without PDMS interlayer. Solid lines in (a) and (b) represent the fitted curves used to estimate resistive and defective features of the devices, respectively. (c) *J-V* characteristics of hole-only devices measured in dark, with arrows indicating the trap-filled limit voltages (V_{TFL}). (d) Schematics of the crosslinking PDMS interlayer.

Fig. 2-9. (Color) Improvements in the photovoltaic performance and air stability of $MAPbI_3$-based solar cells by the PDMS interlayer. (a)

Comparison of PCEs without and with PDMS interlayer. (b) *J–V* characteristic (reverse scan) of the solar cell using PDMS interlayer, with a steady-state current under the maximum power voltage. (c) Shelf-life test of solar cells stored in ambient air (25°C, ~55% relative humidity). (d) Photographs of ITO/SnO_2/$MAPbI_3$/CuSCN/Au devices without and with PDMS interlayer dipped in water.

Fig. 2-10. (Color) Improved performance of $MAPbI_3$-based solar cells by PDMS. *J-V* curves of $MAPbI_3$-based solar cells with (a) reverse and (b) forward scans, and (c) their stabilized power outputs measured at the maximum power voltages.

Fig. 2-11. (Color) Performance of $MAPbI_3$-based solar cells, without and with PDMS. Comparison of the cell parameters including (a) η, (b) J_{SC}, (c) V_{OC}, and (d) *FF* for ~10 devices each.

Fig. 2-12. (Color) Stabilities of $MAPbI_3$-based solar cells and their XRD patterns before/after the stability tests. (a) Stabilities tested under 25°C/~55% RH condition and (b,c) XRD patterns of solar cells with and without PDMS interlayer. (d-f) Data analyzed for the solar cells stored under 25°C/95% RH conditions and (g-i) under 85°C/35% RH conditions. All the tests were conducted for solar cells without encapsulation.

Fig. 2-13. (Color) Photovoltaic performance and thermal stability of CsFAMA-based solar cells with and without PDMS interlayer. *J-V* characteristics of triple-cation perovskite

under the maximum power voltage, (c) hysteresis index (HI = 1-η_{FOR}/η_{REV}), and (d) external quantum efficiency of the perovskite solar cells.

Fig. 3-9. (Color) Optimization of the Cu_2O and CuSCN concentrations of nanocomposite based devices. Comparison of the performances for 7 devices at each condition. The optimum condition is 10 mg/ml for both Cu_2O and CuSCN.

Fig. 3-10. (Color) The *J-V* plot of the device with a bilayer-deposited HTL**.** The perovskite solar cells were fabricated by the following sequence: 10 mg/ml of Cu_2O-dispersion solution was spin coated on a perovskite film, then 10 mg/ml of CuSCN solution was deposited subsequently.Fig. 3-11. (Color) Long-term stability of the solar cells with different HTLs. (a) Thermal stability of the devices, and (b) XRD of the devices stored under 85°C/85% RH for 720 h (with gold removed before the diffraction measurements).

Fig. 3-12. (Color) Long-term stability for several devices with different HTLs. (a) Normalized η, (b) η, (c) J_{SC}, (d) V_{OC}, (e) *FF*, and (h) *HI* of the devices stored under 85°C/85% RH with encapsulation in dark condition.

Chapter 1.
Overview

1.1. Introduction to Solar Cells

The basic principle of operation of solar cells is the photovoltaic effect. When the light reaches the device, the electrons on the valance band are excited to a higher energy state by absorbing photon energy greater than the energy band gap of the material leaving the holes in the valance band (Fig. 1-1). When these photon energy absorptions occur in the space charge region, the excited electrons and holes are spatially separated by a built-in field that causes a net current through the junction. Carriers excited by photon energy greater than the band gap of the material are cooled to a state near the band edge through a phonon interaction called thermalization (①). The excited carrier can make radiative recombination (②) with carriers of opposite charge directly (③) or trap-assisted (④) with releasing photons before extraction into an external circuit. Charge carriers (electrons and holes) are extracted into the external circuit by diffusion (⑤) or trapped at near-surface defect sites making non-radiative recombination (⑥).[1] In open circuit conditions, a photovoltaic voltage is generated from the separated quasi-Fermi level between *p*-type and *n*-type materials. Defect sites such as point defects, dislocations usually located at surfaces, and grain boundaries create in-band conditions that act as trap sites for charge carriers and advance non-radioactive recombination. In order to build an efficient solar cell from the above operating principle, using materials with adequate band gap and sufficient light absorption coefficient, efficient charge separation and drift, diffusion to the electrodes. Moreover, minimizing defect density to reduce the non-radioactive recombination is

important to develop efficient and stable solar cells.[2]

Power conversion efficiency (η) is defined as the ratio between the maximum power output ($V_{MPP} \times J_{MPP}$) of a solar cell and the incident power of solar energy shown in Fig. 1-2. It is determined by three quantities: short circuit current density (*Jsc*), open circuit voltage (*Voc*) and charge factor (*FF*). *Jsc* is a measurement of charge generation and transfer to subsequent external circuitry. For high *Jsc*, the material must satisfy the balance between incident photon extinction and light carrier extraction, and have low band gap to reduce the spectrum loss. For high *Voc*, wide bandgap materials have an advantage to obtain high separated quasi-Fermi level, which is the dilemma between current and voltage, causing photocurrent loss due to forbidden excitation in the bandgap. The fill factor is the ratio between η and the multiplication of *Jsc* and *Voc*.

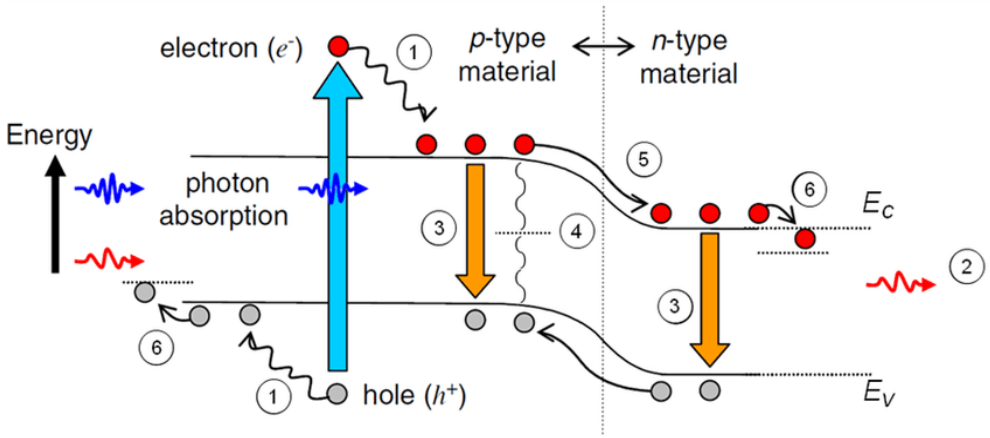

Fig. 1-1. (Color) Working process and energy loss of *p*-*n* junction solar cells. From Ref. [1].

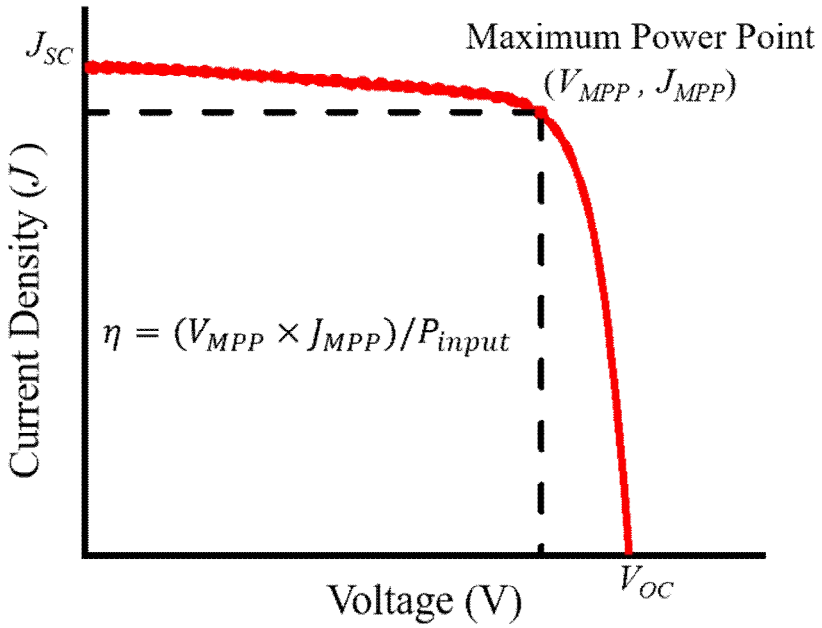

Fig. 1-2. (Color) A Schematic of a *J-V* curve and photovoltaic parameters.

1.2. Organic-Inorganic Hybrid Perovskite (OHP) Solar Cells

Organic-inorganic hybrid perovskites (OHPs) normally have a ABX_3 perovskite structure containing organic or inorganic cations ($CH_3NH_3^+$ (MA), $(NH_2)_2CH^+$ (FA), Cs^+) at A site, inorganic cations (Pb^{2+} or Sn^{2+}) at B site, and halide anions (Cl^-, Br^-, or I^-) at X site. Since the 2009 when OHP solar cells (PSCs) have been reported, η of PSCs is rapidly increased compared to other types of solar cells (from 3.8% to 25.2%), closely reaching to the theoretical Shockely-Queisser limit shown in Fig. 1-3.[3] One of remarkable merit points of OHP is the solution-processible-film deposition. Precursor is prepared by dissolving constituent compounds (e.g., MAI and PbI_2 for $MAPbI_3$) in a common solvent (e.g., DMSO and DMF) forming intermediate crystalline phase (e.g., MAI-DMSO-PbI_2). The solvent was subsequently spin coated, then the polycrystalline OHP film is developed from the intermediate phase during thermal annealing. The anti-solvent (e.g., diethylether or chlorobenzene) is normally dripped during the spin coating to enhance the OHP quality, resulting in the compact and uniform film on the substrate.[4] Not only OHPs show outstanding properties including a high absorption coefficient and carrier mobility and a low exciton binding energy, but also tunable bandgap energy by facile composition modification is most notable part for fabricate efficient PSCs.[5,6]

As solar cells show layered structure, OHP film is deposited between each selective materials, *n*-type for electron transport layer (ETL) and *p*-type for hole transport layer (HTL) shown in Fig. 1-4. The criteria for good selective contact for PSCs are not limiting the photovoltaic

performance, good energy level alignment of each layers, and high charge mobility. Efficient charge transfer at each interfaces and the suppressing the reverse transfer are required for the maximum extraction of electrons and holes from photo-absorption layer to charge-extraction layers. Two types of device are commonly fabricated, i.e. *n-i-p* planar and *p-i-n* inverted structure. For the planar structure, light penetrates into the ETL while it is the HTL in the inverted structure. Transparent oxide semiconductor is used as an *n*-type in the planar (e.g., TiO_2, SnO_2, and ZnO) and *p*-type in the inverted structure (e.g., PEDOT:PSS, CuO, and NiO). Small or polymeric molecular is used as HTL in the planar (e.g., Spiro-OMeTAD and PTAA) and ETL in the inverted structure (e.g., PCBM). For the upper layer deposition on hybrid perovskite, it certainly requires the solvent that is inactive to perovskite since the vulnerability to the polar solvent causes the decomposition into PbI_2 (e.g., H_2O, alcohol, DMF, DMSO, and acetone). Selective contact also provides the physical barrier by hampering the diffusion of atmospheric reactive elements (e.g., humid and O_2), and therefore the protective property is additionally considered to hinder the degradation of OHP film.

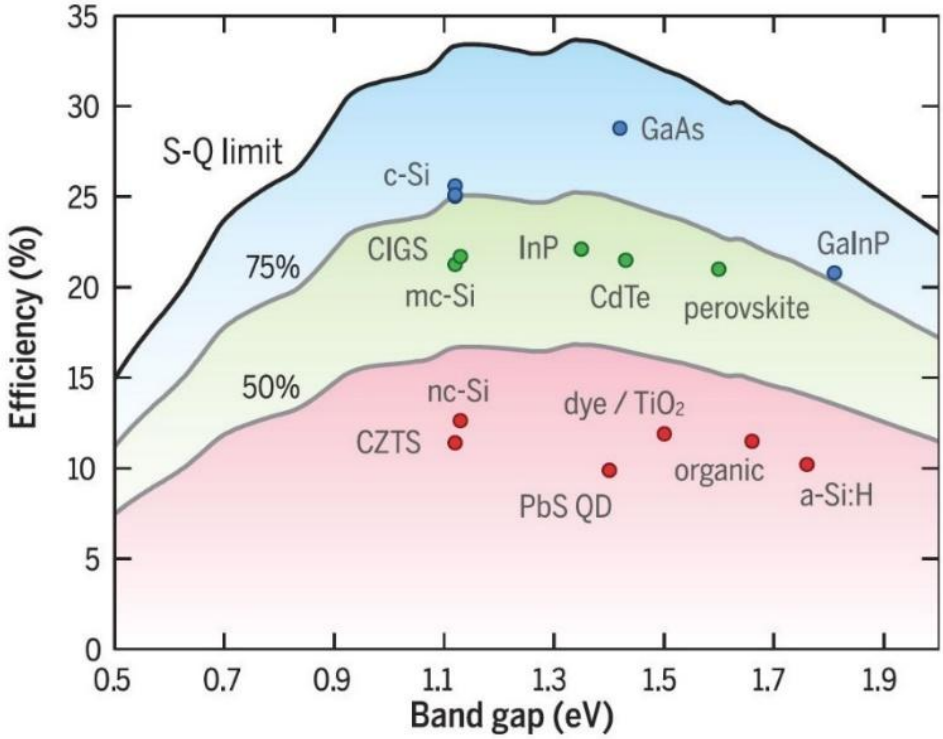

Fig. 1-3. (Color) Shockley-Queisser efficiency limits and experimental efficiencies of solar cells with various materials. From Ref. [3].

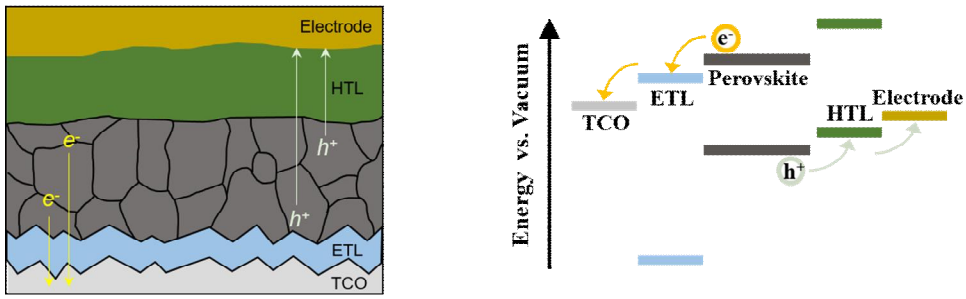

Fig. 1-4. (Color) A schematic device architecture and band structure of *n-i-p* planar type perovskite solar cells.

1.3. Issues of Performance and Stability in OHP Solar Cells

Non-radiative recombination during PSCs working is main degradation of the photovoltaic efficiency, and trap states from deep and shallow level defects act as recombination center for charge carriers.[7] Vacancy is one of major defects in OHP film accompanies high density of trap states, and the formation of defects at the OHP is thought to greatly influence not only the photovoltaic performance but also its long-term stability of PSCs being major factor in the degradation of PSCs (Fig. 1-5).[8] Various studies to reduce defect density have been widely studied, and there are two strategies for suppressing vacancies. Additives like Cs+ and F- at the perovskite precursor are used for reducing defect sites usually existing at surface and grain boundary.[9,10] Defect passivation by Lewis base or Lewis acid via π-conjugation between B site of OHP and Lewis adduct is also widely applied.[11-13]

Ambient condition with heat and humidity is also the major factor for the degradation of PSCs. The volatile property of organic compounds in OHP makes perovskite easily dissociate under heat and humidity induced environment as shown in Fig. 1-6.[14] Moreover, OHP degradation under heat induced condition is inflicted by dopants and additives required for small molecule or polymer hole transport materials because of its low hole mobility compared to the inorganic materials (Fig. 1-7).[15] Due to the thermal stability issues of organic hole transport materials, *p*-type metal oxides (e.g., CuO, Cu_2O, $CuGaO_2$, NiO) have been tried for efficient and stable PSCs because of its high hole mobility and conductivity without any dopants (Table 1-1).[16-22] There were many attempts to long-term

stability of PSCs, yet the intrinsic property of OHP and selective layers should be further investigated to compete against the other types of solar cells.

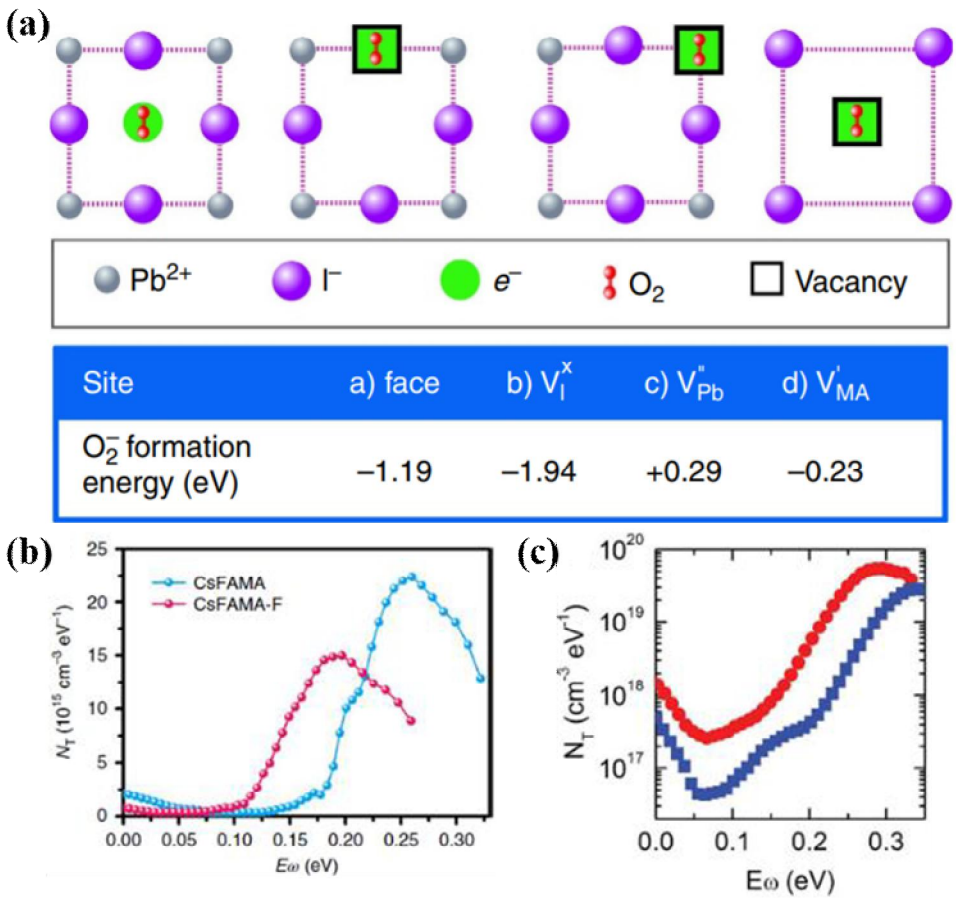

Fig. 1-5. (Color) (a) Proposed defect sites via vacancies of OHP. From Ref. 8. (b) $(Cs_{0.05}FA_{0.54}MA_{0.41})Pb(I_{0.98}Br_{0.02})_3$ films with (red circle) and without NaF additive (blue circle). From Ref. [9]. (c) $FAPbI_3$ films with (blue squire) and without Cs doping (red circle). From Ref. [10].

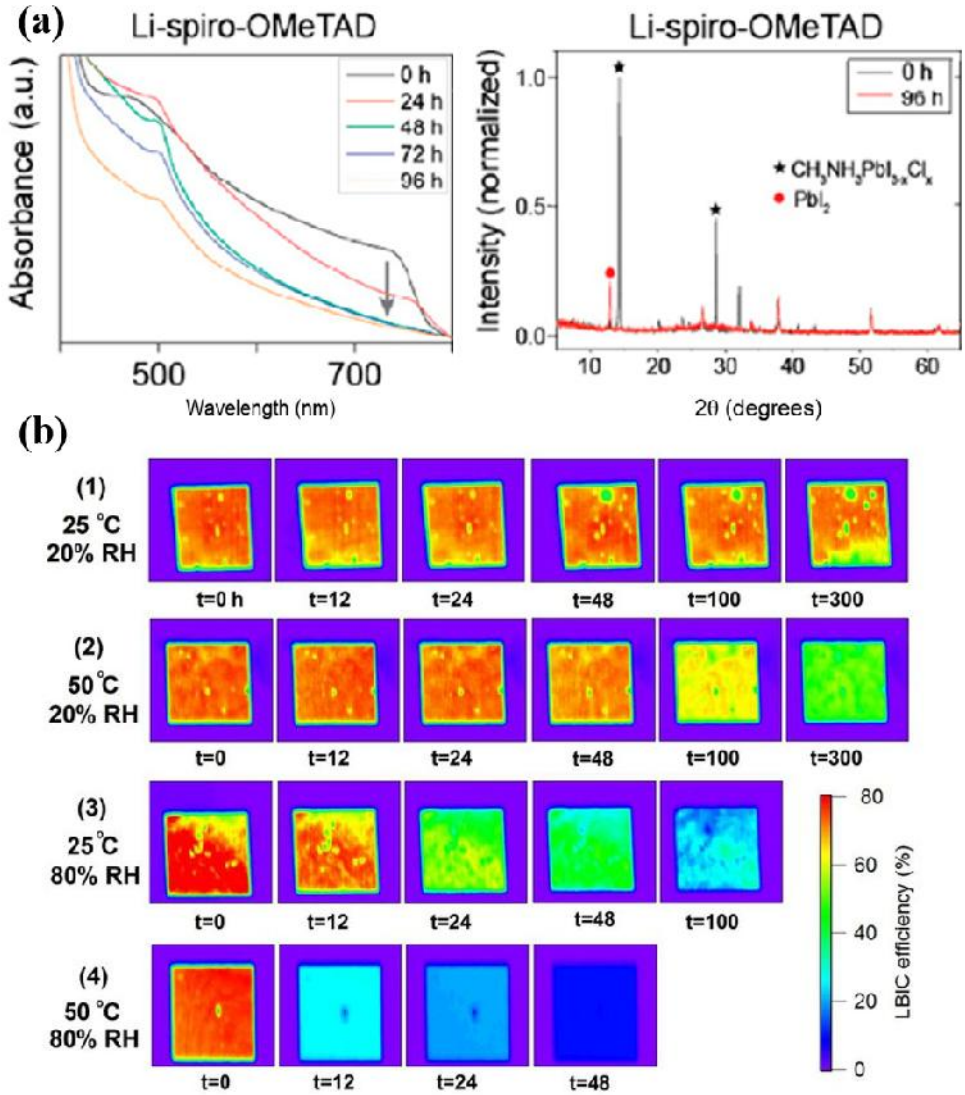

Fig. 1-6. (Color) Perovskite degradation under thermal and humid induced condition. (a) UV-Vis spectrum and XRD of OHP film with various stored times under thermal induced condition. (b) Light beam induced current (LBIC) with various thermal and humid environments. From Ref. [14].

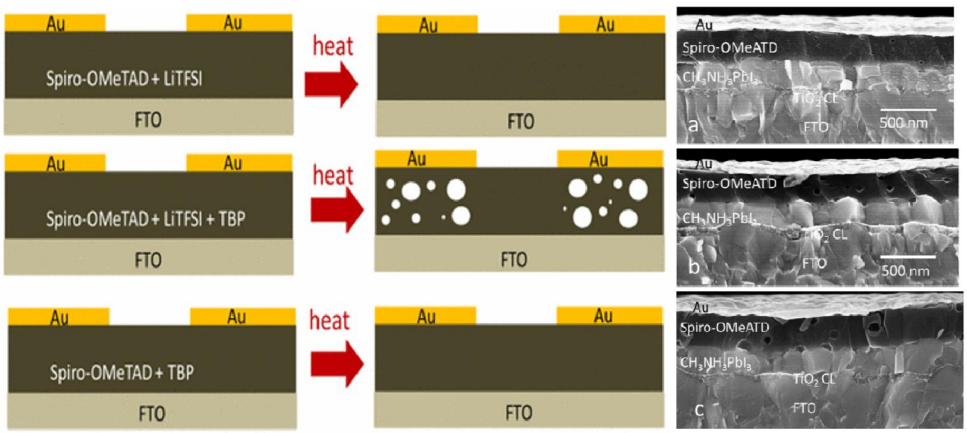

Fig. 1-7. (Color) Thermal degradation of PSCs utilized Spiro-OMeTAD and salt dopants as a hole transport materials. From Ref. [15].

HTM	**Mobility ($cm^2/V \cdot s$)**	**Conductivity (S/cm)**
Spiro-OMeTAD (doped)	$\sim 10^{-4}$ (thin film, TOF and SCLC)[16]	$\sim 5 \times 10^{-5}$ [21]
CuSCN	$\sim 10^{-2} - 10^{-1}$ (thin film, field-effect mobility) [17]	$\sim 9 \times 10^{-5}$ [21]
NiO_x	$\sim 10^{-4}$ (nanoparticulated thin film, SCLC) [18]	$\sim 7 \times 10^{-8}$ [22]
Cu_2O	$\sim 10^{0}$ (nanoparticulated thin film, SCLC)[19]	$\sim 5 \times 10^{-1}$ [19]
$CuGaO_2$	$\sim 10^{-1}$ (nanoparticulated thin film, Hall measurement)[20]	$\sim 5 \times 10^{-3}$ [20]

Table 1-1. Hole mobility and conductivity for several *p*-type materials. From Refs. [16-22].

1.4. References

[1] Arnaoutakis, G. E. Novel Up-Conversion Concentrating Photovoltaic Concepts (Doctors Thesis). Heriot-Watt University, Edinburgh, Scotland.

[2] Dupre, O.; Vaillon, R.; Green, M. A. Physics of the Temperature Coefficients of Solar Cells. *Sol Energ. Mater. Sol. C.* **2015**, *140*, 92-100.

[3] Vossier, A.; Gualdi, F.; Dollet, A.; Ares, R.; Aimez, V. Approaching the Shockley-Queisser Limit: General Assessment of the Main Limiting Mechanisms in Photovoltaic Cells. *J. Appl. Phys.* **2015**, *117*, 015102.

[4] Jeon, N. J.; Noh, J. H.; Kim, Y. C.; Yang, W. S.; Ryu, S.; Seok, S. I. Solvent Engineering for High-Performance Inorganic-Organic Hybrid Perovskite Solar Cells. *Nat. Mater.* **2014**, *13*, 897-903.

[5] Saliba, M.; Matsui, T.; Donamski, K.; Seo, J.-Y.; Ummadisingu, A.; Zakeeruddin, S. M.; Correa-Baena, J.-P.; Tress, W. R.; Abate, A.; Hagfeldt, A.; Gratzel, M. Incorporation of Rubidium Cations into Perovskite Solar Cells Improves Photovoltaic Performance. *Science* **2016**, *354*, 206-209.

[6] Lee, J.-W.; Kim, D.-H.; Kim, H.-S.; Seo, S.-W.; Cho, S. M.; Park, N.-G. Formamidinium and Cesium Hybridization for Photo- and Moisture-Stable Perovskite Solar Cell. *Adv. Energy Mater.* **2015**, *5*, 1501310.

[7] Ball J. M.; Petrozza, A. Defects in Perovskite-Halides and Their Effects in Solar Cells. *Nat. Energy* 2016, **1**, 16149.

[8] Aristidou, N.; Eames, C.; Sanchez-Molina, I.; Bu, X.; Kosco, J.; Islam, M. S.; Haque, S. A. Fast Oxygen Diffusion and Iodide Defects Mediate Oxygen-Induced Degradation of Perovskite Solar Cells. *Nat. Commun.* **2017**, *8*, 15218.

[9] Li, N.; Tao, S.; Chen, Y.; Niu, X.; Onwudinanti, C. K.; Hu, C.; Qiu, Z.; Xu, Z.; Zheng, G.; Wang, L.; Zhang, Y.; Li, L.; Liu, H.; Lun, Y.; Hong, J.; Wang, X.; Liu, Y.; Xie, H.; Gao, Y.; Bai, Y.; Yang, S.; Brocks, G.; Chen, Q.; Zhou, H. Cation and Anion Immobilization through Chemical Bonding Enhancement with Fluorides for Stable Halide Perovskite Solar Cells. *Nat. Energy*, 2019, **4**, 408–415.

[10] Lee, J.-W.; Kim, D.-H.; Kim, H.-S.; Seo, S.-W.; Cho, S. M.; Park, N.-G. Formamidinium and Cesium Hybridization for Photo- and Moisture-Stable Perovskite Solar Cell. *Adv. Energy Mater.* 2015, **5**, 1501310.

[11] Lin, Y.; Shen, L.; Dai, J.; Deng, Y.; Wu, Y.; Bai, Y.; Zheng, X.; Wang, J.; Fang, Y.; Wei, H.; Ma, W.; Zeng, X. C.; Zhan, X.; Huang, J. π-Conjugated Lewis Base: Efficient Trap-Passivation and Charge-Extraction for Hybrid Perovskite Solar Cells. *Adv. Mater.* **2017**, *29*, 1604545.

[12] Yin, W.-J.; Shi, T.; Yan, Y. Unusual Defect Physics in CH3NH3PbI3 Perovskite Solar Cell Absorber. *Appl. Phys. Lett.* **2014**, *10*, 063903.

[13] Zohar, A.; Levine, I.; Gupta, S.; Davidson, O.; Azulay, D.; Milo, O.; Balberg, I.; Hodes, G.; Cahan, D. What is the Mechanism of MAPbI3 p-doping by I2? Insights from Optoelectronic Properties. *ACS Energy Lett.* **2017**, *2*, 2408-2414.

[14] Habisreutinger, S. N.; Leijtens, T.; Eperon, G. E.; Stranks, S. D.;

Nicholas, R. J.; Sanith, H. J. Carbon Nanotube/Polymer Composites as a Highly Stable Hole Collection Layer in Perovskite Solar Cells. *Nano Lett.* **2014**, *14*, 5561-5568.

[15] Jena, A. K.; Ikegami, M.; Miyasaka, T. Severe Morphological Deformation of Sspiro-OMeTAD in $(CH_3NH_3)PbI_3$ Solar Cells at High Temperature. *ACS Energy Lett.* **2017**, *2,* 1760.

[16] Kumekawa, Y.; Hirai, M.; Kobayashi, Y.; Endoh, S.; Oikawa. E.; Hashimoto, T. Evaluation of thermodynamic and kinetic stability of $CuAlO_2$ and $CuGaO_2$. *J. Ther. Anal. Calorim.* **2010**, *99*, 57.

[17] Choulis, S. A.; Nelson, J.; Kim, Y.; Poplavskyy, D.; Kreouzis, T.; Durrant, J. R.; Bradley, D. D. C. Investigation of transport properties in polymer/fullerene blends using time-of-flight photocurrent measurements. *Appl. Phys. Lett.* **2003**, *83*, 3812.

[18] Sha, W. E. I.; Ren, X.; Chen, L.; Choy, W. C. H. The efficiency limit of $CH_3NH_3PbI_3$ perovskite solar cells. *Appl. Phys. Lett.* **2015**, *106*, 221104.

[19] Yu, W.; Li, F.; Wang, H.; Alarousu, E.; Chen, Y.; Lin, B.; Wang, L.; Hedhili, M. N.; Li, Y.; Wu, K.; Wang, X.; Mohammed, O. F.; Wu, T. Ultrathin Cu_2O as an efficient inorganic hole transporting material for perovskite solar cells. *Nanoscale* **2016**, *8*, 6173.

[20] Cao, J.; Yu, H.; Zhou, S.; Qin, M.; Lau, T.-K.; Lu, X.; Zhao, N.; Wong, C.-P. Low-temperature solution-processed NiO_x films for air-stable perovskite solar cells. *J. Mater. Chem. A* **2017**, *5*, 11071.

[21] Leijtens, T.; Giovenzana, T.; Habisreutinger, S. N.; Tinkham, J. S.; Noel, N. K.; Kamino, B. A.; Sadoughi, G.; Sellinger, A.; Snaith, H. J. Hydrophobic Organic Hole Transporters for Improved Moisture

Resistance in Metal Halide Perovskite Solar Cells. *ACS Appl. Mater. Interfaces* **2016**, *8*, 5981.

[22] Li, J.; Zhang, G.; Sun, R.; Wong, C.-P. A covalently cross-linked reduced functionalized graphene oxide/polyurethane composite based on Diels–Alder chemistry and its potential application in healable flexible electronics. *J. Mater. Chem. A* **2017**, *5*, 220.

Chapter 2.
Interfacial Modification and Defect Passivation by Crosslinking Interlayer for Efficient and Stable CuSCN-Based Perovskite Solar Cell

2.1. Introduction

Attentions on the photovoltaics have rapidly grown with the concern of future energy supply.[1-5] Among the various materials and designs, the perovskite solar cell (PSC) has been one of the most popular research objects due to its outstanding potential as the next generation photovoltaics.[6-14] The power conversion efficiency (PCE) of PSC has soared up from 3.8% to 25.2% within several years, and extensive studies for its commercialization are on progress.[14-26] Even though the PCE growth is quite satisfactory, the stability of device is yet below the industrial standard, demanding more advances in materials and designs.

In general, perovskite solar cell has hierarchical structure of perovskite with electron-transport layer (ETL) and hole-transport layer (HTL), and the spiro-OMeTAD is one of the most common material for the HTL.[20-23,25-30] This organic material enables outstanding PCE, but has low stability due to its high reactivity and the salt dopants.[31-35] To overcome the limitation of organic-based HTL, various inorganic *p*-type semiconductors such as metal oxides and copper-based materials have been recently introduced.[36-45]

Among them, CuSCN is one of the promising inorganic materials for the HTL, which has decent hole mobility of 10^{-1} cm^2 V^{-1} s^{-1} enabling solar cells with high theoretical and experimental PCEs.[36-38,43,46-49]

However, despite of its great potential, the deposition of CuSCN with polar solvents still remains as a challenge in the *n-i-p* structured PSC. As diethyl sulfide (DES) is the most common solvent for the solution-deposition of CuSCN, the polar property of DES is reported to induce damages on the perovskite surface.[43,50] The decomposition of organic-inorganic perovskite due to its high reactivity to the polar solvents and consequential trap formation have been reported.[43,50,51] The formation of defects at the interface is thought to greatly influence not only the photovoltaic performance but also its long-term stability, considering that the degradation of CuSCN has been observed with the formation of CuI at the perovskite/CuSCN interface.[38] Therefore, a novel strategy to prevent the degradation of perovskite during the CuSCN deposition and mitigating the trap formation at the interface will play a significant role realizing efficient and stable perovskite solar cells.

Herein, we utilize the PDMS ($CH_3[Si(CH_3)_2O]_nSi(CH_3)_3$) polymers for an interlayer between the perovskite and CuSCN to stabilize the film deposition and device operation. PDMS is a super hydrophobic and thermally resistive polymer,[52-55] and the presence of PDMS interlayer successfully blocks the decomposition of perovskite at the surface during the deposition of upper layer. Also, these PDMS polymers are observed to play a unique role as a crosslinking interlayer, forming chemical bonds with perovskite and CuSCN. This novel linking behavior boosts the hole-extraction property at the interface, and mitigates the interfacial traps/defects in the device. As well known, the defect characteristics at the interface have significant impacts on both the photovoltaic performance and operational stability of PSC. The PDMS crosslinking interlayer greatly

increases the PCE of CuSCN-based PSC from 17.21% to 19.04% (highest efficiencies), and remarkably enhances the device stability against heat and humidity. Further discussion for the effects of PDMS interlayer on the air- and thermal- stabilities of PSC highlights the importance of defect control in realizing stable PSC, and suggests an insight for the ideal design of PSC with inorganic CuSCN HTL.

2.2. Experimental Section

Device Fabrication: ITO substrate (AMG) was etched by zinc powder (TCI Chemicals) and cleaned by sonication in acetone, ethanol and deionized water, for 20 min respectively. The substrate was used after 15 min of UV-ozone treatment. A SnO_2 colloidal dispersion (15 wt. % in water, Alfa Aesar) was diluted to 2.5 wt. % with DI water, and then spin coated on the ITO substrate followed by annealing at 120°C for 30 min. The substrate for hole-only device was fabricated by spin-coating PTAA solution (2 mg/ml in chlorobenzene) on ITO glass with spin rate of 5000 rpm for 40 s, followed by the annealing step at 120°C for 20 min. For the $MAPbI_3$ perovskite film, 1.92 M $MAPbI_3$ perovskite precursor was prepared by dissolving methylammonium iodide (MAI; Great Solar Laboratory), lead iodide (PbI_2; TCI Chemicals) in a mixture of *N*,*N*-dimethylformamide (DMF; Sigma-Aldrich) and dimethylsulfoxide (DMSO; Sigma-Aldrich) with the volume ratio of 9:1. In case of $Cs_{0.05}(FA_{0.83}MA_{0.17})_{0.95}Pb(I_{0.83}Br_{0.17})_3$ perovskite (CsFAMA) film, formamidinium iodide (FAI; Great Solar Laboratory), methylammonium bromide (MABr; Great Solar Laboratory), PbI_2 and lead bromide ($PbBr_2$; TCI Chemicals) were dissolved in DMF/DMSO with 4:1 volume ratio with

the addition of CsI/DMSO solution. The perovskite solution was spin-coated at 3000 rpm for 20 s (with 1 mL of diethyl ether used as an antisolvent). PDMS (Sigma Aldrich) interlayer was prepared by dissolving 12.25 mg of PDMS in 1 mL of *n*-Hexane (Daejung) then spin-coated on the perovskite film. Hole transporting material was prepared by dissolving 25 mg of CuSCN (Sigma Aldrich) in 1 mL of diethylsulfide (Sigma Aldrich) then spin-coated on the substrate followed by annealing at 50°C for 10 min.

Characterization: Optical properties of perovskite films were measured with UV/Vis spectroscopy (V-770; JASCO) with an integrating sphere. Crystal structures of perovskite were examined by an x-ray diffractometer (New D-8 Advance; Bruker). To observe the cross-sectional image of devices, a field-emission scanning electron microscope (Merlin Compact; Zeiss) was used. Raman and steady-state photoluminescence spectra were obtained via LabRAM HV Evolution, Horiba, using lasers of $\lambda_{excitation}$ = 325 and 532 nm. Time-resolved PL spectra (FluoTime 300; Picoquant) were obtained using $\lambda_{excitation}$ = 398 nm laser. The films were prepared on glass substrates with the incident light direction on the perovskite or CuSCN surface. Time-of-flight secondary-ion mass spectroscopy (TOF.SIMS-5; ION-TOF) was performed to analyze the compositional depth profile of PDMS-interlayered device. Four-point probe was utilized to measure the electric conductivity of films deposited on quartz substrates. Work functions of films were measured via multipurpose x-ray photoelectron spectroscopy (Sigma Probe; Thermo VG Scientific), conducted with argon sputtering, and photon energy of hv = 21.22 eV was used in the ultraviolet photoelectron spectroscopy (UPS)

measurement. A potentiostat (Zive SP-1; WonATech) was adopted for both space-charge-limited current (SCLC) analysis and impedance analysis. For the SCLC measurement, voltage was applied from 0 V to 10 V. The impedance of photovoltaic device was measured with 10 mV AC perturbation in the frequency range from 10 mHz to 100 kHz, under zero bias in dark condition. Before this measurement, all the devices had been relaxed in dark until voltage drops below 3 mV. Photocurrent density-voltage (*J-V*) curves were achieved via solar cell measurement system (K-3000; McScience) for an active area of 0.09 cm^2. During the measurement, the voltage was swept from the reverse to forward direction (from 1.2 to −0.1 V with a scan rate of 100 mV s^{-1}). One sun light was illuminated using a solar simulator (Xenon lamp, air mass 1.5 G).

2.3. Results and Discussion

To clarify the degradation of perovskite layer during the CuSCN deposition, the $MAPbI_3$/CuSCN films are investigated with different pre-wetting time of CuSCN solution from 0 to 90 s followed by a spin-coating step. As the CuSCN solution is wetted longer on the perovskite substrate, the degradation of perovskite occurs more severely at a level that can be easily compared visually. The features of each film including optical images, absorbance spectra and x-ray diffraction patterns are compared in the Supporting Information, Fig. 2-1. With clear evidence of the surface degradation, it is necessary to improve the quality of perovskite/CuSCN interface.

As an ideal strategy to suppress the perovskite decomposition, a buffer interlayer is designed with super hydrophobic PDMS, and the perovskite

surface is successfully protected from the damage by CuSCN-DES solution (Fig. 2-2). In addition, polymers with hydrophobic property are also expected to boost the stability of solar cell without hindering its photovoltaic performance, regarding that the utilization of hydrophobic upper layer is reported to improve the device stability under humid air.[56,57] Furthermore, polymers with lone pair of electrons are reported to passivate defects forming Lewis adduct with perovskite,[58,59] indicating the possible passivation of the interfacial defects by PDMS. The schematics with cross-sectional SEM images for the synthesis of CuSCN-based PSCs is shown in Fig. 2-3. It should be noted that 200-nm PDMS layer looks diminished after the deposition of CuSCN. Since PDMS is also soluble in DES solvent, most of the PDMS polymers are dissolved and removed during the CuSCN deposition step.

To certify the existence of residual PDMS and their role at the interface, samples are analyzed through Raman spectroscopy, as shown in Fig. 2-4(a). While the $MAPbI_3$/CuSCN films do not show notable differences compared with the bare $MAPbI_3$ (with signals near 100 cm^{-1} originating from $MAPbI_3$), $MAPbI_3$/PDMS/CuSCN exhibits two distinctive peaks near 135 and 280 cm^{-1} which represent the bonds of Pb-O and Cu-O, respectively.[60,61] These peaks confirm that the residual PDMS polymers at the interface remain chemically bonded with both perovskite and CuSCN. In addition, time-of-flight secondary-ion mass spectroscopy (ToF-SIMS) is employed to examine the compositional depth profiles for the $MAPbI_3$/PDMS/CuSCN sample. As demonstrated in Fig. 2-4(a), Si signals from the PDMS polymers are identified near the interface. From the results of ToF-SIMS and Raman spectroscopy, we assume that most of

PDMS polymers exist at the interface strongly holding two distinct layers as a crosslinking interlayer. This crosslinking behavior of PDMS interlayer may play a significant role in the performance of PSC, and further analyses are conducted to scrutinize the effects of PDMS interlayer on various properties of the solar cell.

The PDMS polymers basically have insulating property which can hinder the charge extraction and transfer at the interface. Therefore, the photoluminescence (PL) spectroscopy has been conducted for each structure deposited on a glass substrate to compare the hole-extraction property from perovskite to the CuSCN HTL. As shown in Fig. 2-4(b), a PL peak at 766 nm is identified for every case, which represents the radiative recombination of excitons in $MAPbI_3$. Without any electrode in contact, bare $MAPbI_3$ shows strong PL intensity with majority of photocarriers dissipating via radiative recombination. On the other hand, with CuSCN as an upper layer, a large proportion of holes are extracted into the CuSCN HTL resulting in the decreased PL intensity. Notably, when PDMS interlayer is incorporated, more effective PL quenching is observed, implying that holes are effectively extracted into the CuSCN HTL. The time-resolved PL (TRPL) has been also measured, where $MAPbI_3$/PDMS/CuSCN shows more rapid PL decay compared to the $MAPbI_3$/CuSCN sample. The PL decay curves are fitted to the biexponential functions, and the average carrier lifetime is significantly reduced with the PDMS interlayer, implying the improved hole-extracting properties by PDMS/CuSCN HTL. In addition, even though the PDMS itself has deficient electrical properties, the PDMS/CuSCN film shows negligible decreases in both electrical conductivity and hole mobility as shown in Fig. 2-5 and Fig. 2-6.

Considering that the energy level of CuSCN remains unchanged with or without PDMS interlayer (Fig. 2-7), the utilization of PDMS crosslinking interlayer barely blocks the carrier transfer but rather improves the photovoltaic property.

Regarding that the PDMS interlayer affects carrier dynamics at the interface in a positive manner, analyzing and comparing the formation of interfacial traps will provide further insight to understand the role of PDMS. Therefore, the impedance analysis is conducted for the CuSCN-based solar cells with and without PDMS interlayer, and the corresponding Nyquist plots are depicted in Fig. 2-8(a). The PDMS/CuSCN device shows larger hemi-circle than that of the bare CuSCN device, which infers greater resistive factor of the charge recombination process in solar cells.[62,63] These Nyquist data indicate that the PDMS interlayer reduces the trap/defect sites near the interface. For more reliable and quantitative analysis, the trap distribution spectra are obtained, as shown in Fig. 2-8(b). This trap analysis is one of the valid and useful methods to investigate the electronic-trap distribution at the interfaces, with details discussed in several reports.[51,64-68] The spectra of deep traps at the interface vividly show the differences in the CuSCN solar cells with and without PDMS interlayer. The energy level of traps drastically shifts toward the bandedge by over 0.1 eV with the PDMS interlayer. In addition, the PDMS/CuSCN device shows only half trap density (N_t) compared to the bare CuSCN device.

In order to reconfirm the defect-passivation effect by PDMS interlayer, the dark current to voltage characteristics for hole-only devices are measured. The *J-V* curves of ITO/PTAA/$MAPbI_3$/HTL/Au devices are shown in Fig. 2-8(c), and the trap densities are estimated from the trap-filled

limit voltage (V_{TFL}) to be 3.4×10^{15} cm^{-3} and 9.2×10^{15} cm^{-3} for the devices with and without PDMS interlayer, respectively.[69,70] The PDMS clearly reduces the hole-trap density at the $MAPbI_3$/CuSCN interface, which is a consistent result with that from the impedance analysis above. Reduction of the electronic traps suggests that by using the PDMS interlayer, the formation of deep traps at the perovskite/CuSCN interface can be mitigated reducing the undesirable charge recombination, which will contribute to the enhanced hole-extraction and improved photovoltaic parameters.[50] We rationally attribute the change in the trap states not only because the PDMS interlayer acts as a buffer layer preventing the perovskite decomposition by CuSCN-DES solution, but also because the crosslinking behavior of PDMS polymers further passivates traps/defects, such as ion vacancies or dangling bonds of both perovskite and CuSCN by binding with Pb and Cu atoms (Fig. 2-8(d)).

Then perovskite devices of ITO/SnO_2/$MAPbI_3$/CuSCN/Au are fabricated with and without PDMS interlayer, and its influence on the actual photovoltaic performance has been scrutinized. As demonstrated in Figs. 2-9(a), 2-10 and 2-11, the solar cells with PDMS interlayers show dramatic improvement in photovoltaic parameters including short-circuit current (J_{SC}), open-circuit voltage (V_{OC}) and fill factor (FF), and consequently the power-conversion efficiency (η) is increased from 17.21% to 19.04% (highest efficiencies). The J-V characteristics and stabilized power output of the best performing PDMS/CuSCN device are shown in Fig. 2-9(b). It is noteworthy that by the straightforward insertion of PDMS interlayer via solution-process, highly efficient CuSCN-based PSC has been realized with PCE comparable to that of the organic HTL-based PSCs.

In our previous work, we have confirmed that reduction of the interfacial deep traps plays a significant role enhancing V_{OC} and J_{SC} by mitigating nonradiative recombination at the interface, which causes loss in both V_{OC} and charge extractions.[51,66] Recalling that the electronic trap states are considerably reduced as observed by impedance analysis and *J-V* characteristics in Fig. 2-8, improved photovoltaic performance of PDMS devices are majorly due to the mitigation of interfacial traps by the PDMS crosslinking interlayer. Better hole-extraction efficiency of PDMS/CuSCN HTL observed by PL analyses in Fig. 2-4(b) is also believed to play an important role in improving J_{SC} and η.

Furthermore, the PDMS interlayer improves the air stability. The PDMS-interlayered PSC maintains its performance stable at 25°C/over-55% relative humidity (RH) for more than 1000 h without any encapsulation (Fig. 2-9(c)). The PDMS/CuSCN device also endures extreme humidity (95% RH), much better than the bare CuSCN device (Fig. 2-12). It is astonishing that the device with PDMS sustains the perovskite layer protected even when dipped in water, while the device without PDMS interlayer immediately turns yellow due to the decomposition of $MAPbI_3$ into PbI_2 (Fig. 2-9(d)). It confirms that the interlayer of PDMS suppresses the penetration/diffusion of external H_2O molecules through the interface.

Due to the facile decomposition of $MAPbI_3$ under heat condition (Fig. 2-12), triple-cation perovskite $Cs_{0.05}(FA_{0.83}MA_{0.17})_{0.95}Pb(I_{0.83}Br_{0.17})_3$ (CsFAMA) is utilized as an active material for the thermal stability test. As shown in Figs. 2-13 and 2-14, clear improvements in the solar cell performance using PDMS interlayer is observed (ITO/SnO_2/CsFAMA/CuSCN/Au) as well. As stored under rigorous

condition of 85°C/85% RH with encapsulation, the device with PDMS interlayer retains 90% of its initial PCE for 500 h, while the PCE of bare CuSCN device drops severely during the first 100 h of storage. By achieving such a drastic improvement in the thermal stability of CuSCN-based PSC using PDMS crosslinking interlayer, it is persuasive that the defect state at the interface between perovskite and CuSCN is one of the dominant factors which controls thermal degradation in the device. Considering that PDMS interlayer passivates the traps/defects, which is also supported by the reduced *J-V* hysteresis of devices (Fig. 2-15), the reduction of trap/defect sites may prevent the interdiffusion of ionic defects through the interface under the thermal stress.

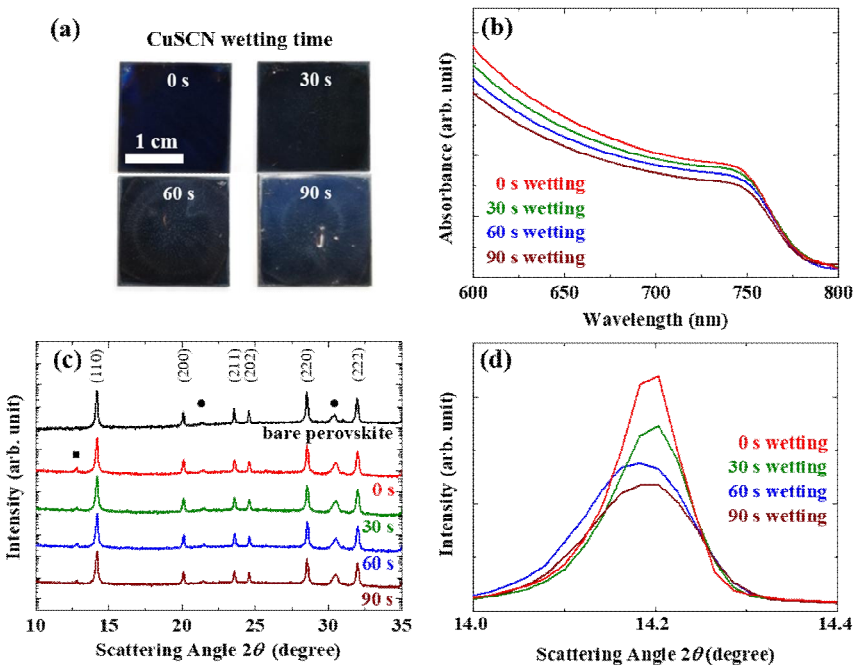

Fig. 2-1. (Color) Observation of the perovskite degradation by CuSCN-diethyl sulfide (DES) solution. (a) Optical images, (b) absorbance spectra, and (c) XRD patterns of ITO/SnO_2/$MAPbI_3$/CuSCN films with different wetting times (from 0 to 90 s) of CuSCN-DES solution. The square and circles in (c) represent the peaks of PbI_2 and ITO, respectively. (d) Comparison of the magnified peaks at 14.2° (for the (110) plane in $MAPbI_3$).

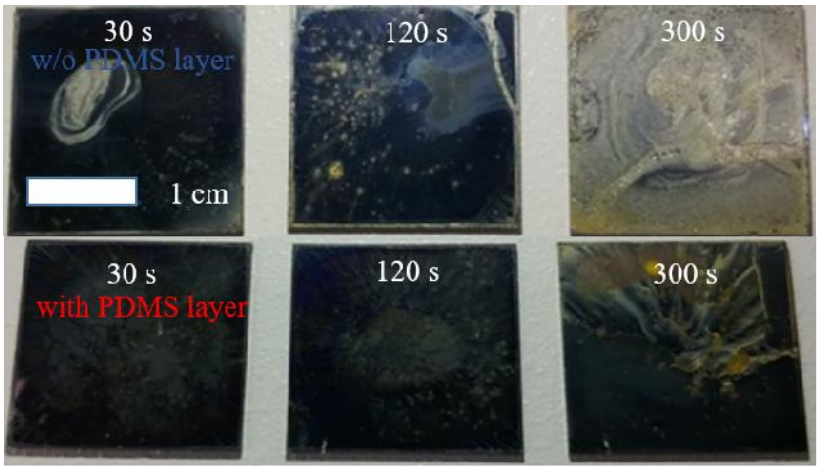

Fig. 2-2. (Color) Compared degradation of perovskite by CuSCN-DES solution. Optical images of ITO/SnO_2/$MAPbI_3$/PDMS/CuSCN films with different wetting times of CuSCN-DES solution, without and with PDMS buffer layer.

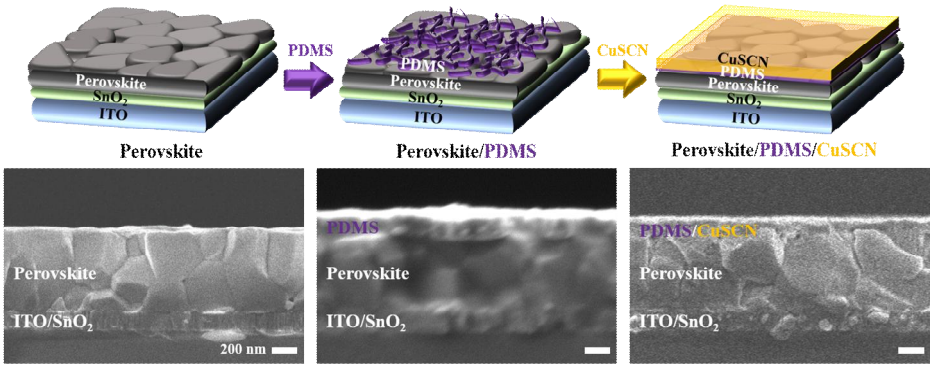

Fig. 2-3. (Color) Solution-processed deposition for the PDMS interlayer and CuSCN HTL. Schematic architectures and the cross-sectional SEM images of ITO/SnO_2/perovskite, ITO/SnO_2/perovskite/PDMS, and ITO/SnO_2/perovskite/PDMS/CuSCN.

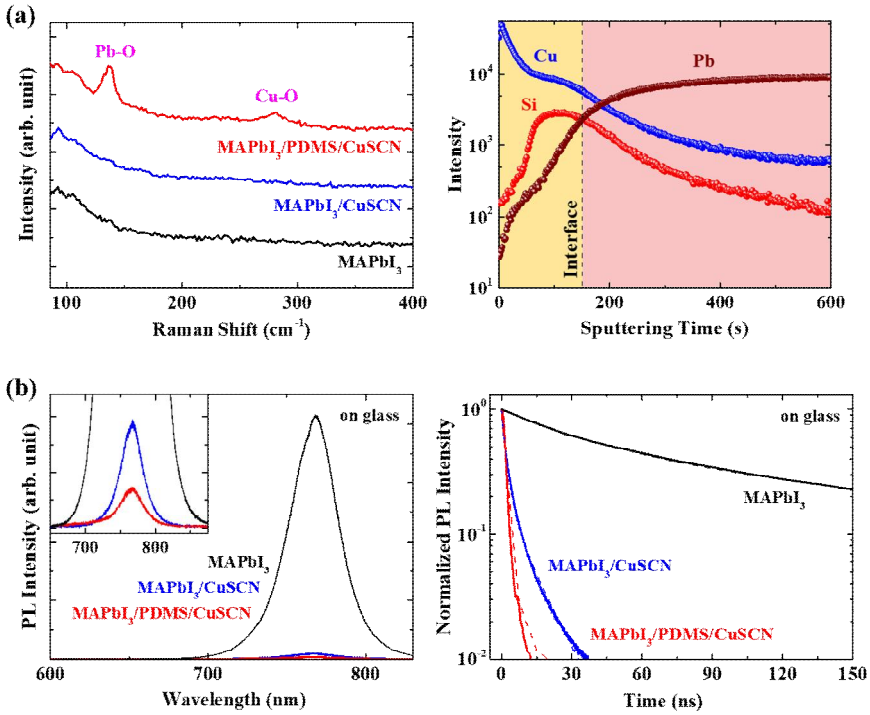

Fig. 2-4. (Color) Analyses on the PDMS interlayer and charge-extraction properties by different HTLs. (a) Raman spectra with different HTLs and ToF-SIMS depth profile analysis for the PDMS-interlayered device. (b) Steady-state PL spectra with magnified image (inset), and time-resolved PL of various films deposited on a glass substrate. Dashed lines represent the fitted curves.

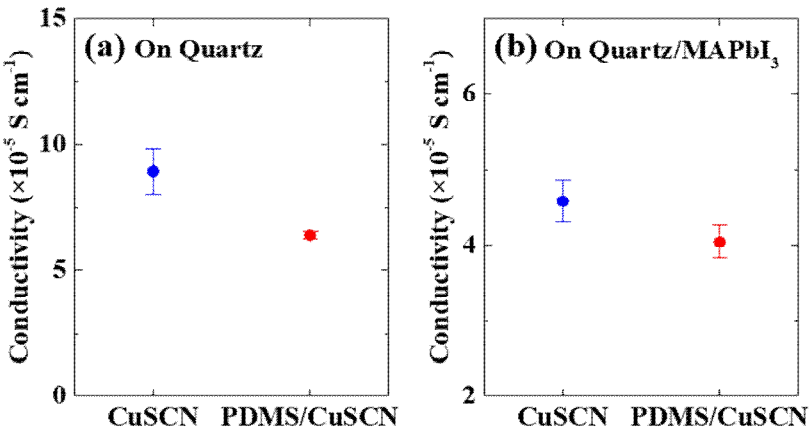

Fig. 2-5. (Color) Electrical properties of CuSCN and PDMS/CuSCN films. Sheet resistance is measured by four-point probe for CuSCN and PDMS/CuSCN films, which are deposited on (a) quartz substrates and (b) $MAPbI_3$ films.

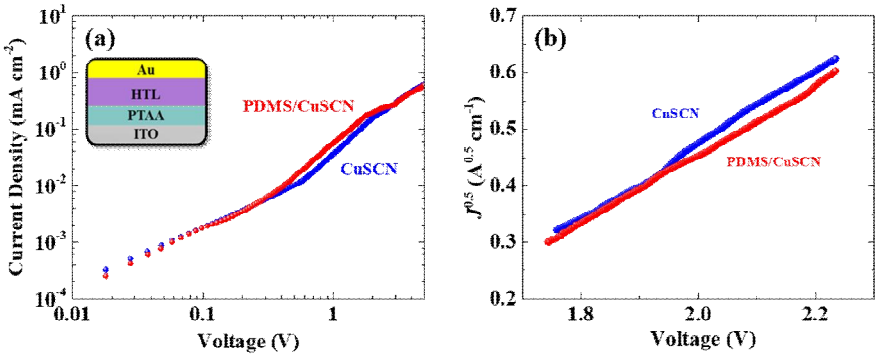

Fig. 2-6. (Color) Space-charge limited current (SCLC) measured for CuSCN and PDMS/CuSCN films. (a) *J-V* characteristics of hole-only devices without perovskite layer, measured in dark condition. (b) $J^{0.5}$-V plot in the SCLC region with high applied voltage. The hole mobilities μ_h are calculated to be 0.20 and 0.18 cm^2 V^{-1} s^{-1}, for CuSCN and PDMS/CuSCN films respectively.

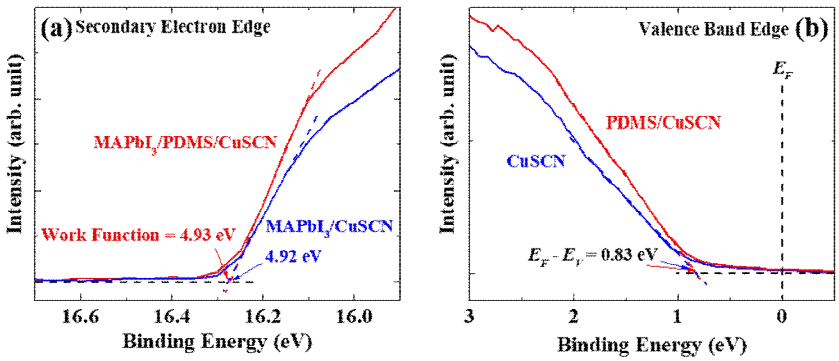

Fig. 2-7. (Color) Ultraviolet photoemission spectroscopy measurement for various surfaces. Photoemission spectra for (a) secondary electron edge and (b) valence band edge on the surfaces of CuSCN HTLs with and without PDMS interlayer.

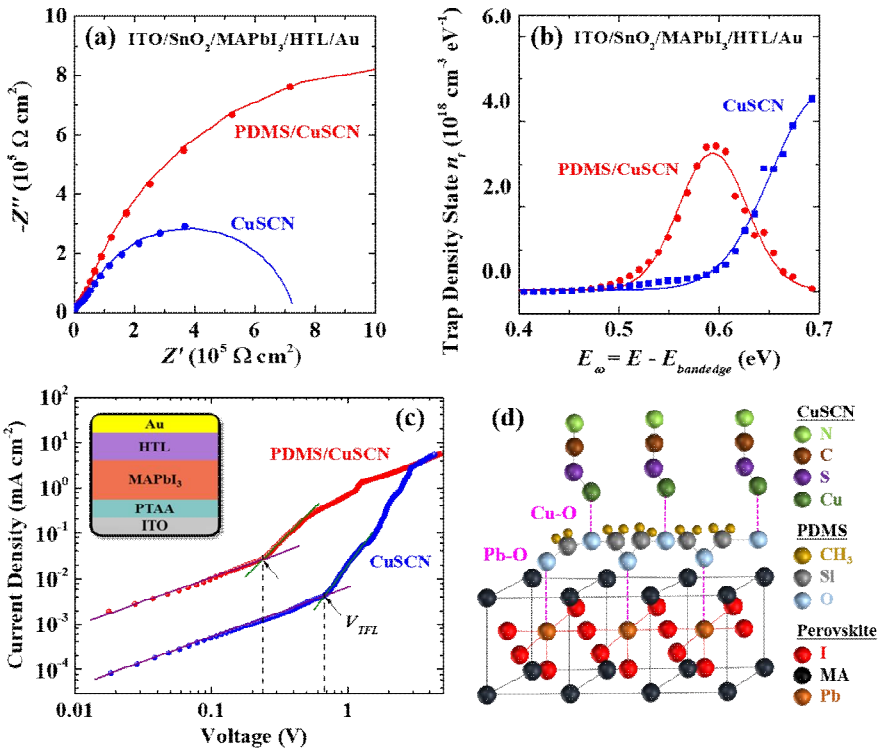

Fig. 2-8. (Color) Passivation of defects by the PDMS interlayer. (a) Nyquist plots and (b) trap distribution spectra of the $MAPbI_3$/CuSCN-based PSCs with and without PDMS interlayer. Solid lines in (a) and (b) represent the fitted curves used to estimate resistive and defective features of the devices, respectively. (c) *J-V* characteristics of hole-only devices measured in dark, with arrows indicating the trap-filled limit voltages (V_{TFL}). (d) Schematics of the crosslinking PDMS interlayer.

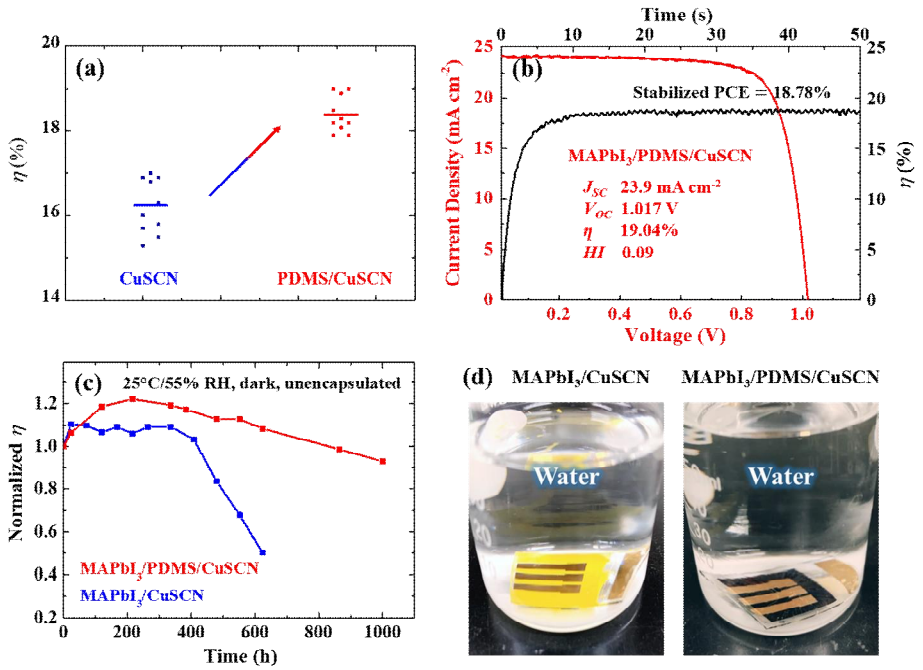

Fig. 2-9. (Color) Improvements in the photovoltaic performance and air stability of $MAPbI_3$-based solar cells by the PDMS interlayer. (a) Comparison of PCEs without and with PDMS interlayer. (b) *J–V* characteristic (reverse scan) of the solar cell using PDMS interlayer, with a steady-state current under the maximum power voltage. (c) Shelf-life test of solar cells stored in ambient air (25°C, ~55% relative humidity). (d) Photographs of ITO/SnO_2/$MAPbI_3$/CuSCN/Au devices without and with PDMS interlayer dipped in water.

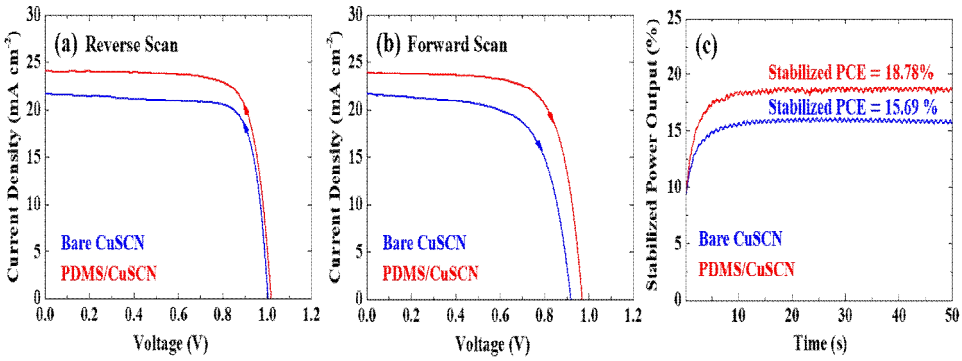

Fig. 2-10. (Color) Improved performance of $MAPbI_3$-based solar cells by PDMS. *J-V* curves of $MAPbI_3$-based solar cells with (a) reverse and (b) forward scans, and (c) their stabilized power outputs measured at the maximum power voltages.

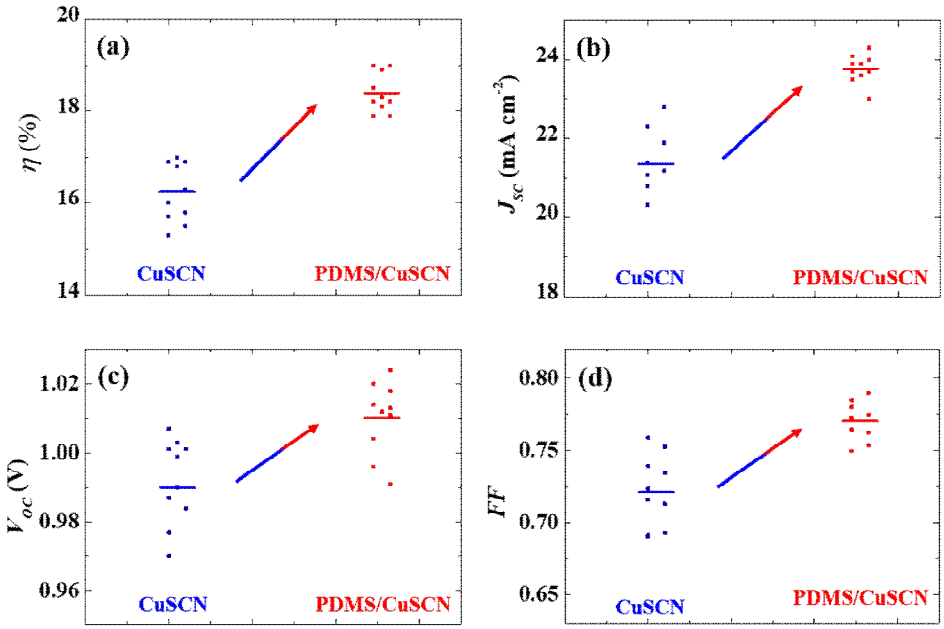

Fig. 2-11. (Color) Performance of $MAPbI_3$-based solar cells, without and with PDMS. Comparison of the cell parameters including (a) η, (b) J_{SC}, (c) V_{OC}, and (d) FF for ~10 devices each.

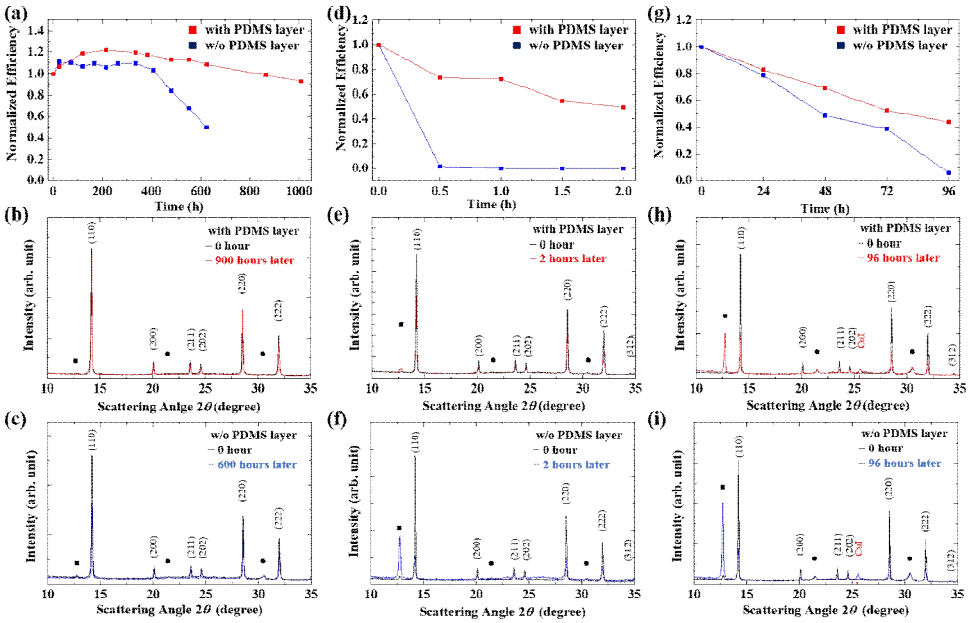

Fig. 2-12. (Color) Stabilities of $MAPbI_3$-based solar cells and their XRD patterns before/after the stability tests. (a) Stabilities tested under 25°C/~55% RH condition and (b,c) XRD patterns of solar cells with and without PDMS interlayer. (d-f) Data analyzed for the solar cells stored under 25°C/95% RH conditions and (g-i) under 85°C/35% RH conditions. All the tests were conducted for solar cells without encapsulation.

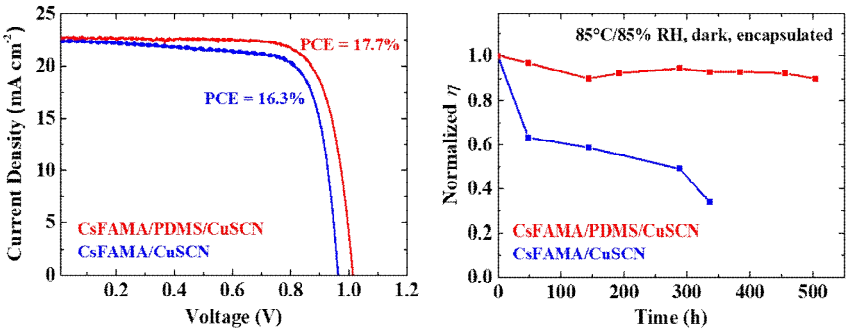

Fig. 2-13. (Color) Photovoltaic performance and thermal stability of CsFAMA-based solar cells with and without PDMS interlayer. *J-V* characteristics of triple-cation perovskite ($Cs_{0.05}(FA_{0.83}MA_{0.17})_{0.95}Pb(I_{0.83}Br_{0.17})_3$: CsFAMA)-based devices, and thermal stability of the encapsulated solar cells stored under 85°C/85% RH condition.

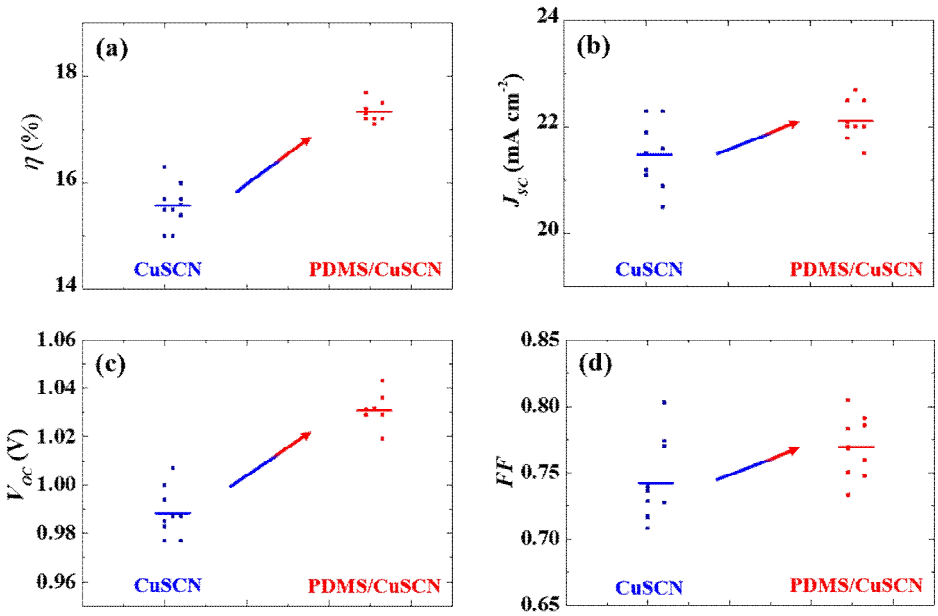

Fig. 2-14. (Color) Performance of $Cs_{0.05}(FA_{0.83}MA_{0.17})_{0.95}Pb(I_{0.83}Br_{0.17})_3$/CuSCN-based devices. (a) η, (b) J_{SC}, (c) V_{OC}, and (d) FF of CsFAMA/CuSCN-based solar cells without and with PDMS interlayer.

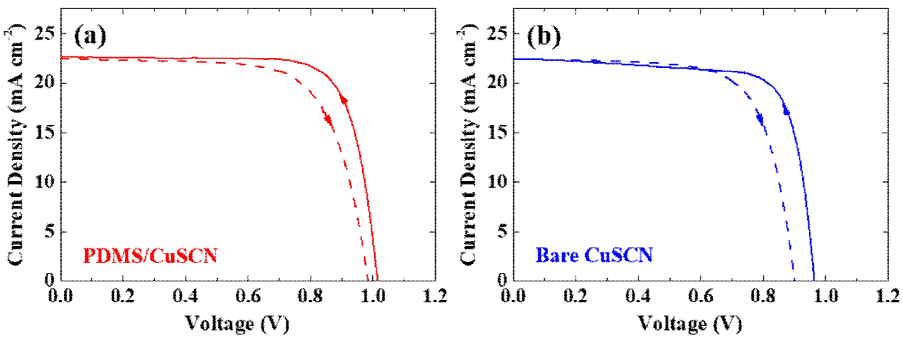

Fig. 2-15. (Color) Device performance of CsFAMA-based solar cells. *J-V* curves of triple-cation perovskite ($Cs_{0.05}(FA_{0.83}MA_{0.17})_{0.95}Pb(I_{0.83}Br_{0.17})_3$: CsFAMA)-based solar cells (a) with and (b) without PDMS interlayer.

2.4. Conclusions

Herein, we suggest the PDMS interlayer as an ideal and facile strategy to prevent the interfacial degradation of the perovskite in the CuSCN-based PSC. We have fabricated PDMS interlayer by a simple solution-process, and most importantly, identified a crosslinking behavior of PDMS polymers at the interface. The chemical bonds formed by PDMS polymers are believed to mitigate traps/defects at the interface, improving the photovoltaic performance of the device with the enhanced hole-extraction property. The PDMS crosslinking interlayer enables highly efficient CuSCN-based PSC with PCE over 19.0%, which is among the top levels reported so far. Moreover, the PDMS-modified interface allows the solar cell to maintain over 90% of its initial PCE both after 1000 h storage under ambient condition (25°C/over-55% RH, unencapsulated) and after 500 h storage under rigorous condition (85°C/85% RH, encapsulated). Further studies on the correlation between the defect states of PDMS-interlayered PSC and its degradation will provide the insights to realize commercialization of highly stable PSC.

2.5. References

[1] Grandidier, J.; Callahan, D. M.; Munday, J. N.; Atwater, H. A. Light Absorption Enhancement in Thin-Film Solar Cells Using Whispering Gallery Modes in Dielectric Nanospheres. *Adv. Mater*. 2011, *23*, 1272-1276.

[2] Shin, B.; Zhu, Y.; Gunawan, O.; Bojarczuk, N. A.; Chey, S. J.; Guha, S. Thin Film Solar Cell with 8.4% Power Conversion Efficiency

Using an Earth-Abundant Cu_2ZnSnS_4 Absorber. *Prog. Photovolt: Res. Appl*. 2013, *21*, 72-76.

[3] Park, H. H.; Heasley, R.; Sun, L.; Steinmann, V.; Jaramillo, R.; Hartman, K.; Chakraborty, R.; Sinsermsuksakul, P.; Chua, D.; Buonassisi, T.; Gordon, R. G. Co-Optimization of SnS Absorber and Zn (O, S) Buffer Materials for Improved Solar Cells. *Prog. Photovolt: Res. Appl*. 2015, *23*, 901-908.

[4] Lee, S.; Flanagan, J. C.; Lee, B.; Hwang, T.; Kim, J.; Gil, B.; Shim, M.; Park, B. Route to Improving Photovoltaics Based on $CdSe/CdSe_xTe_{1-x}$ Type-II Heterojunction Nanorods: The Effect of Morphology and Cosensitization on Carrier Recombination and Transport. *ACS Appl. Mater. Interfaces* 2017, *9*, 31931- 31939.

[5] Lee, S.; Flanagan, J. C.; Kim, J.; Yun, A. J.; Lee, B.; Shim, M.; Park, B. Efficient Type-II Heterojunction Nanorod Sensitized Solar Cells Realized by Controlled Synthesis of Core/Patchy-Shell Structure and CdS Cosensitization. *ACS Appl. Mater. Interfaces* 2019, *11*, 19104-19114.

[6] Snaith, H. J. Perovskites: The Emergence of a New Era for Low-Cost, High-Efficiency Solar Cells. *J. Phys. Chem. Lett*. 2013, *4*, 3623-3630.

[7] Hodes, G. Perovskite-Based Solar Cells. *Science* 2013, *342*, 317-318.

[8] Ponseca, Jr., C. S.; Savenije, T. J.; Abdellah, M.; Zheng, K.; Yartsev, A.; Pascher, T.; Harlang, T.; Chabera, P.; Pullerits, T.; Stepanov, A.; Wolf, J.-P.; Sundstrom, V. Organometal Halide Perovskite Solar Cell Materials Rationalized: Ultrafast Charge Generation, High and Microsecond-Long Balanced Mobilities, and Slow Recombination. *J. Am. Chem. Soc.* 2014, *136*, 5189-5192.

[9] Frost, J. M.; Butler, K. T.; Brivio, F.; Hendon, C. H.; Schilfgaarde, M. v.; Walsh, A. Atomistic Origins of High-Performance in Hybrid Halide Perovskite Solar Cells. *Nano Lett*. 2014, *14*, 2584-2590.

[10] Lee, B.; Lee, S.; Cho, D.; Kim, J.; Hwang, T.; Kim, K. H.; Hong, S.; Moon, T.; Park, B. Evaluating the Optoelectronic Quality of Hybrid Perovskites by Conductive Atomic Force Microscopy with Noise Spectroscopy. *ACS Appl. Mater. Interfaces* 2016, *8*, 30985-30991.

[11] Kim, J.; Hwang, T.; Lee, S.; Lee, B.; Kim, J.; Kim, J.; Gil, B.; Park, B. Synergetic Effect of Double-Step Blocking Layer for the Perovskite Solar Cell. *J. Appl. Phys*. 2017, *122*, 145106.

[12] Xu, Q.; Yang, D.; Lv, J.; Zhang, L. Perovskite Solar Absorbers: Materials by Design. *Small Methods* 2018, *2*, 1700316.

[13] Hwang, T.; Lee, B.; Kim, J.; Lee, S.; Gil, B.; Yun, A. J.; Park, B. From Nanostructural Evolution to Dynamic Interplay of Constituents: Perspectives for Perovskite Solar Cells. *Adv. Mater*. 2018, *30*, 1704208.

[14] Xu, X. Z.; Zhang, X. J.; Deng, W.; Jie, J. S.; Zhang, X. H. 1D Organic–Inorganic Hybrid Perovskite Micro/Nanocrystals: Fabrication, Assembly, and Optoelectronic Applications. *Small Methods* 2018, *2*, 1700340.

[15] NREL, Best Research-Cell Efficiency Chart. https://www.nrel.gov/pv/cell-efficiency.html (accessed Aug 5 2019).

[16] Kojima, A.; Teshima, K.; Shirai, Y.; Miyasaka, T. Organometal Halide Perovskites as Visible-Light Sensitizers for Photovoltaic Cells. *J. Am. Chem. Soc*. 2009, *131*, 6050-6051.

[17] Berry, J.; Buonassisi, T.; Egger, D. A.; Hodes, G.; Kronik, L.; Loo, Y.-L.; Lubomirsky, I.; Marder, S. R.; Mastai, Y.; Miller, J. S.; Mitzi, D. B.; Paz, Y.; Rappe, A. M.; Riess, I.; Rybtchinski, B.; Stafsudd, O.; Stevanovic, V.; Toney, M. F.; Zitoun, D.; Kahn, A.; Ginley, D.; Cahen, D. Hybrid Organic–Inorganic Perovskites (HOIPs): Opportunities and Challenges. *Adv. Mater.* 2015, *27*, 5102-5112.

[18] Kim, J.; Hwang, T.; Lee, S.; Lee, B.; Kim, J.; Jang, G. S.; Nam, S.; Park, B. Solvent and Intermediate Phase as Boosters for the Perovskite Transformation and Solar Cell Performance. *Sci. Rep*. 2016, *6*, 25648.

[19] Kim, D.; Kim, G. Y.; Ko, C.; Pae, S. R.; Lee, Y. S.; Gunawan, O.; Ogletree, D. F.; Jo, W.; Shin, B. Effects of Postsynthesis Thermal Conditions on Methylammonium Lead Halide Perovskite: Band Bending at Grain Boundaries and Its Impacts on Solar Cell Performance. *J. Phys. Chem. C* 2016, *120*, 21330-21335.

[20] Hwang, T.; Lee, S.; Kim, J.; Kim, J.; Kim, C.; Shin, B.; Park, B. Tailoring the Mesoscopic TiO_2 Layer: Concomitant Parameters for Enabling High-Performance Perovskite Solar Cells. *Nanoscale Res. Lett.* 2017, *12*, 57.

[21] Wu, Z.; Li, P.; Zhang, Y.; Zheng, Z. Flexible and Stretchable Perovskite Solar Cells: Device Design and Development Methods. *Small Methods* 2018, *2*, 1800031

[22] Wieghold, S.; Correa-Baena, J.-P.; Nienhaus, L.; Sun, S.; Shulenberger, K. E.; Liu, Z.; Tresback, J. S.; Shin, S. S.; Bawendi, M. G.; Buonassisi, T. Precursor Concentration Affects Grain Size, Crystal Orientation, and Local Performance in Mixed-Ion Lead Perovskite Solar Cells. *ACS Appl. Energy Mater.* 2018, *1*, 6801-6808.

[23] Jung, H. J.; Kim, D.; Kim, S.; Park, J.; Dravid, V. P.; Shin, B. Stability of Halide Perovskite Solar Cell Devices: In Situ Observation of Oxygen Diffusion under Biasing. *Adv. Mater.* 2018, *30*, 1802769.

[24] Lee, B.; Shin, B.; Park, B. Uniform Cs_2SnI_6 Thin Films for Lead-Free and Stable Perovskite Optoelectronics via Hybrid Deposition Approaches. *Electron. Mater. Lett.* 2019, *15*, 192-200.

[25] Kim, J.; Hwang, T.; Lee, B.; Lee, S.; Park, K.; Park, H. H.; Park, B. An Aromatic Diamine Molecule as the A-Site Solute for Highly

Durable and Efficient Perovskite Solar Cells. *Small Methods* 2019, *3*, 1800361.

[26] Lee, B.; Hwang, T.; Lee, S.; Shin, B.; Park, B. Microstructural Evolution of Hybrid Perovskites Promoted by Chlorine and its Impact on the Performance of Solar Cell. *Sci. Rep*. 2019, *9*, 4803.

[27] Zhang, H.; Shi, Y.; Yan, F.; Wang, L.; Wang, K.; Xing, Y.; Dong, Q.; Ma, T. A Dual Functional Additive for the HTM Layer in Perovskite Solar Cells. *Chem. Commun.* 2014, *50*, 5020-5022.

[28] Liu, Q.; Fan, L.; Zhang, Q.; Zhou, A.; Wang, B.; Bai, H.; Tian, Q.; Fan, B.; Zhang, T. Benzoyl Peroxide as an Efficient Dopant for Spiro-OMeTAD in Perovskite Solar Cells. *ChemSusChem* 2017, *10*, 3098-3104.

[29] Ko, Y.; Kim, Y.; Lee, C.; Kim, Y.; Jun, Y. Investigation of Hole-Transporting Poly(triarylamine) on Aggregation and Charge Transport for Hysteresisless Scalable Planar Perovskite Solar Cells. *ACS Appl. Mater. Interfaces* 2018, *10*, 11633-11641.

[30] Gu, X.; Li, Y.; Mu, Y.; Zhang, M.; Lu, T.; Wang, P. $FeCl_3$ as a Low-Cost and Efficient *p*-Type Dopant of Spiro-OMeTAD for High Performance Perovskite Solar Cells. *RSC Adv.* 2018, *8*, 9409-9413.

[31] Gratia, P.; Magomedov, A.; Malinauskas, T.; Daskeviciene, M.; Abate, A.; Ahmad, S.; Grätzel, M.; Getautis, V.; Nazeeruddin, M. K. A Methoxydiphenylamine-Substituted Carbazole Twin Derivative: An Efficient Hole-Transporting Material for Perovskite Solar Cells. *Angew. Chem., Int. Ed*. 2015, *54*, 11409-11413.

[32] Kim, G.-W.; Kang, G.; Kim, J.; Lee, G.-Y.; Kim, H. I.; Pyeon, L.; Lee, J.; Park, T. Dopant-Free Polymeric Hole Transport Materials for Highly Efficient and Stable Perovskite Solar Cells. *Energy Environ. Sci.* 2016, *9*, 2326-2333.

[33] Huang, C.; Fu, W.; Li, C.-Z.; Zhang, Z.; Qiu, W.; Shi, M.; Heremans, P.; Jen, A. K.-Y.; Chen, H. Dopant-Free Hole-Transporting Material with a C_{3h} Symmetrical Truxene Core for Highly Efficient Perovskite Solar Cells. *J. Am. Chem. Soc.* 2016, *138*, 2528-2531.

[34] Jena, A. K.; Ikegami, M.; Miyasaka, T. Severe Morphological Deformation of Spiro-OMeTAD in $(CH_3NH_3)PbI_3$ Solar Cells at High Temperature. *ACS Energy Lett.* 2017, *2*, 1760-1761.

[35] Li, Y.; Scheel, K. R.; Clevenger, R. G.; Shou, W.; Pan, H.; Kilway, K. V.; Peng, Z. Highly Efficient and Stable Perovskite Solar Cells Using a Dopant-Free Inexpensive Small Molecule as the Hole-Transporting Material. *Adv. Energy Mater.* 2018, *8*, 1801248.

[36] Jung, M.; Kim, Y. C.; Jeon, N. J.; Yang, W. S.; Seo, J.; Noh, J. H.; Seok, S. I. Thermal Stability of CuSCN Hole Conductor-Based Perovskite Solar Cells. *ChemSusChem* 2016, *9*, 2592-2596.

[37] Yu, W.; Li, F.; Wang, H.; Alarousu, E.; Chen, Y.; Lin, B.; Wang, L.; Hedhili, M. N.; Li, Y.; Wu, K.; Wang, X.; Mohammedc, O. F.; Wu, T. Ultrathin Cu_2O as an Efficient Inorganic Hole Transporting Material for Perovskite Solar Cells. *Nanoscale* 2016, *8*, 6173-6179.

[38] Liu, J.; Pathak, S. K.; Sakai, N.; Sheng, R.; Bai, S.; Wang, Z.; Snaith, H. J. Identification and Mitigation of a Critical Interfacial Instability in Perovskite Solar Cells Employing Copper Thiocyanate Hole-Transporter. *Adv. Mater. Interfaces* 2016, *3*, 1600571.

[39] Huckaba, A. J.; Gharibzadeh, S.; Ralaiarisoa, M.; Roldán-Carmona, C.; Mohammadian, N.; Grancini, G.; Lee, Y.; Amsalem, P.; Plichta, E. J.; Koch, N.; Moshaii, A.; Nazeeruddin, M. K. Low-Cost TiS_2 as Hole-Transport Material for Perovskite Solar Cells. *Small Methods* 2017, *1*, 1700250.

[40] Ali, F.; Khoshsirat, N.; Duffin, J. L.; Wang, H.; Ostrikov, K.; Bell, J. M.; Tesfamichael, T. Prospects of E-Beam Evaporated Molybdenum

Oxide as a Hole Transport Layer for Perovskite Solar Cells. *J. Appl. Phys.* 2017, *122*, 123105.

[41] Cao, J.; Yu, H.; Zhou, S.; Qin, M.; Lau, T.-K.; Lu, X.; Zhao, N.; Wong, C.-P. Low-Temperature Solution-Processed NiO_x Films for Air-Stable Perovskite Solar Cells. *J. Mater. Chem. A* 2017, *5*, 11071-11077.

[42] Zhang, H.; Wang, H.; Chen, W.; Jen, A. K.-Y. $CuGaO_2$: A Promising Inorganic Hole-Transporting Material for Highly Efficient and Stable Perovskite Solar Cells. *Adv. Mater.* 2017, *29*, 1604984.

[43] Arora, N.; Dar, M. I.; Hinderhofer, A.; Pellet, N.; Schreiber, F.; Zakeeruddin, S. M.; Grätzel, M. Perovskite Solar Cells with CuSCN Hole Extraction Layers Yield Stabilized Efficiencies Greater than 20%. *Science* 2017, *358*, 768-771.

[44] Yu, Z.; Sun, L. Inorganic Hole-Transporting Materials for Perovskite Solar Cells. *Small Methods* 2018, *2*, 1700280.

[45] Gil, B.; Yun, A. J.; Lee, Y.; Kim, J.; Lee, B.; Park, B. Recent Progress in Inorganic Hole Transport Materials for Efficient and Stable Perovskite Solar Cells *Electron. Mater. Lett.* 2019, *15*, 505-524.

[46] Wijeyasinghe, N.; Anthopoulos, T. D. Copper(I) Thiocyanate (CuSCN) as a Hole-Transport Material for Large-Area Opto/Electronics. *Semicond. Sci. Technol.* 2015, *30*, 104002.

[47] Madhavan, V. E.; Zimmermann, I.; Roldan-Carmona, C.; Grancini, G.; Buffiere, M.; Belaidi, A.; Nazeeruddin, M. K. Copper Thiocyanate Inorganic Hole-Transporting Material for High-Efficiency Perovskite Solar Cells. *ACS Energy Lett.* 2016, *1*, 1112-1117.

[48] Vivo, P.; Salunke, J. K.; Priimagi, A. Hole-Transporting Materials for Printable Perovskite Solar Cells. *Materials* 2017, *10*, 1087.

[49] Casas, G. A.; Cappelletti, M. A.; Cedola, A. P.; Soucase, B. M.; y Blanca, E. L. P. Analysis of the Power Conversion Efficiency of Perovskite Solar Cells with Different Materials as Hole-Transport

Layer by Numerical Simulations. *Superlattices and Microstructures* 2017, *107*, 136-143.

[50] Yang, I. S.; Sohn, M. R.; Sung, S. D.; Kim, Y. J.; Yoo, Y. J.; Kim, J. H.; Lee, W. I. Formation of Pristine CuSCN Layer by Spray Deposition Method for Efficient Perovskite Solar Cell with Extended Stability. *Nano Energy* 2017, *32*, 414-421.

[51] Hwang, T.; Yun, A. J.; Kim, J.; Cho, D.; Kim, S.; Hong, S.; Park, B. Electronic Traps and Their Correlations to Perovskite Solar Cell Performance via Compositional and Thermal Annealing Controls. *ACS Appl. Mater. Interfaces* 2019, *11*, 6907-6917.

[52] Caminoa, G.; Lomakin, S. M.; Lazzari, M. Polydimethylsiloxane Thermal Degradation Part 1. Kinetic Aspects. *Polymer* 2001, *42*, 2395-2402.

[53] Zheng, L.; Chung, Y.-H.; Ma, Y.; Zhang, L.; Xiao, L.; Chen, Z.; Wang, S.; Qu, B.; Gong, Q. A Hydrophobic Hole Transporting Oligothiophene for Planar Perovskite Solar Cells with Improved Stability. *Chem. Commun*. 2014, *50*, 11196-11199.

[54] Chang, H.; Tu, K.; Wang, X.; Liu, J. Fabrication of Mechanically Durable Superhydrophobic Wood Surfaces Using Polydimethylsiloxane and Silica Nanoparticles. *RSC Adv.* 2015, *5*, 30647-30653.

[55] Kumar, R. S.; Padmanathan, N.; Alagar, M. Design of Hydrophobic Polydimethylsiloxane and Polybenzoxazine Hybrids for Interlayer Low *k* Dielectrics. *New J. Chem*., 2015, *39*, 3995-4008.

[56] Xie, J.; Yu, X.; Sun, X.; Huang, J.; Zhang, Y.; Lei, M.; Huang, K.; Xu, D.; Tang, Z.; Cui, C.; Yang, D. Improved Performance and Air Stability of Planar Perovskite Solar Cells via Interfacial Engineering Using a Fullerene Amine Interlayer. *Nano Energy* 2016, *28*, 330-337.

[57] Liu, Y.; Akin, S.; Pan, L.; Uchida, R.; Arora, N.; Milić, J. V.; Hinderhofer, A.; Schreiber, F.; Uhl, A. R.; Zakeeruddin, S. M.; Hagfeldt, A.; Dar, M. I.; Grätzel, M. Ultrahydrophobic 3D/2D Fluoroarene Bilayer-Based Water-Resistant Perovskite Solar Cells with Efficiencies Exceeding 22%. *Sci. Adv.* 2019, *5*, 2543.

[58] Qin, P. L.; Yang, G.; Ren, Z. W.; Cheung, S. H.; So, S. K.; Chen, L.; Hao, J.; Hou, J.; Li, G. Stable and Efficient Organo-Metal Halide Hybrid Perovskite Solar Cells via π-Conjugated Lewis Base Polymer Induced Trap Passivation and Charge Extraction. *Adv. Mater.* 2018, *30*, 1706126.

[59] Yang, S.; Dai, J.; Yu, Z.; Zhou, Y.; Xiao, X.; Zeng, X. C.; Huang, J. Tailoring Passivation Molecular Structures for Extremely Small Open-Circuit Voltage Loss in Perovskite Solar Cells. *J. Am. Chem. Soc.* 2019, *141*, 5781-5787.

[60] Xu, J. F.; Ji, W.; Shen, Z. X.; Li, W. S.; Tang, S. H.; Ye, X. R.; Jia, D. Z.; Xin, X. Q. Raman Spectra of CuO Nanocrystals. *J. Raman Spectrosc.* 1999, *30*, 413-415.

[61] Burgio, L.; Clark, R. J. H.; Firth, S. Raman Spectroscopy as a Means for the Identification of Plattnerite (PbO_2), of Lead Pigments and of Their Degradation Products. *Analyst* 2001, *126*, 222-227.

[62] Guerrero, A.; Garcia-Belmonte, G.; Mora-Sero, I.; Bisquert, J.; Kang, Y. S.; Jacobsson, T. J.; Correa-Baena, J.-P.; Hagfeldt, A. Properties of Contact and Bulk Impedances in Hybrid Lead Halide Perovskite Solar Cells Including Inductive Loop Elements. *J. Phys. Chem. C* 2016, *120*, 8023-8032.

[63] Wang, S.; Zhu, Y.; Wang, C.; Ma, R. Interface Modification by a Multifunctional Ammonium Salt for High Performance and Stable Planar Perovskite Solar Cells. *J. Mater. Chem. A* 2019, *7*, 11867-11876.

[64] Prochowicz, D.; Yadav, P.; Saliba, M.; Saski, M.; Zakeeruddin, S. M.; Lewinski, J.; Grätzel, M. Reduction in the Interfacial Trap Density of Mechanochemically Synthesized $MAPbI_3$. *ACS Appl. Mater. Interfaces* 2017, *9*, 28418-28425.

[65] Li, N.; Tao, S.; Chen, Y.; Niu, X.; Onwudinanti, C. K.; Hu, C.; Qiu, Z.; Xu, Z.; Zheng, G.; Wang, L.; Zhang, Y.; Li, L.; Liu, H.; Lun, Y.; Hong, J.; Wang, X.; Liu, Y.; Xie, H.; Gao, Y.; Bai, Y.; Yang, S.; Brocks, G.; Chen, Q.; Zhou, H. Cation and Anion Immobilization through Chemical Bonding Enhancement with Fluorides for Stable Halide Perovskite Solar Cells. *Nat. Energy* 2019, *4*, 408-415.

[66] Yun, A. J.; Kim, J.; Hwang, T.; Park, B. Origins of Efficient Perovskite Solar Cells with Low-Temperature Processed SnO_2 Electron Transport Layer. *ACS Appl. Energy Mater.* 2019, *2*, 3554-3560.

[67] Hwang, T.; Yun, A. J.; Lee, B.; Kim, J.; Lee, Y.; Park, B. Methylammonium-Chloride Post-Treatment on Perovskite Surface and Its Correlation to Photovoltaic Performance in the Aspect of Electronic Traps. *J. Appl. Phys*. 2019, *126*, 023101.

[68] Kim, J.; Yun, A. J.; Gil, B.; Lee, Y.; Park, B. Triamine-Based Aromatic Cation as a Novel Stabilizer for Efficient Perovskite Solar Cells. *Adv. Funct. Mater.* 2019, *29*, 1905190.

[69] Bube, R. H. Trap Density Determination by Space-Charge-Limited Currents. *J. Appl. Phys.* 1962, *33*, 1733–1737.

[70] Tang, G.; You, P.; Tai, Q.; Yang, A.; Cao, J.; Zheng, F.; Zhou, Z.; Zhao, J.; Chan, P. K. L.; Yan, F. Solution-Phase Epitaxial Growth of Perovskite Films on 2D Material Flakes for High-Performance Solar `Cells. *Adv. Mater.* 2019, *31*, 1807689.

Chapter 3.
Cu_2O-CuSCN Nanocomposite as a Hole-Transport Material of Perovskite Solar Cells for Enhanced Carrier Transport and Suppressed Surface Degradation

3.1. Introduction

Interest in solar power increases as concerns about future energy supplies keep growing.[1-5] In the midst of the numerous solar cells, perovskite solar cells (PSCs) gathered much attention due to its potential for the next generation energy resources.[6-14] Organohalide perovskite (OHP) obtains outstanding nature of an appropriate and direct bandgap, small exciton-binding energy, and balanced ambipolar charge transport properties, resulting in high PCE.[15-24] However, organohalide framework of OHP results unstable features, resulting in material degradation or interfacial reaction. Even though material stability is largely improved throughout extensive works, interfacial reaction still remains to be controlled. Especially, stability of hole-transporting material (HTL) causes large issue, because of the unstable behavior of organic-based HTL interacting with perovskite layer.[25-32]

Due to the interfacial degradation of perovskite and HTL, inorganic HTLs were extensively investigated, and the CuSCN-based HTL resulted in high PCE and improved stability compared to organic-based HTLs.[33-41] Although CuSCN itself is stable material, halides in OHP migrate to the CuSCN interface, forming an improper copper halides and defects in OHP.[39] Recently, interlayers were investigated to reduce the interfacial reaction between OHP and CuSCN, and metal oxides or organics were also

considered as options to improve stability.[42,43] However, deposition of metal oxides requires polar solvent, damaging the perovskite layer, and organics can degrade under the heat-induced condition. Therefore, utilization of complex design is highly required.

Among many different metal oxides, Cu_2O is the one of the ideal materials with outstanding hole mobility and appropriate valence-band maximum.[44-48] Several articles reported the synthesis of Cu_2O as an HTL for the *p-i-n* type PSCs, but those methods used polar solvent and high-temperature heat treatment which are not suitable for *n-i-p* type PSCs.[49-51] In the case of the *n-i-p* type PSCs, dispersed Cu_2O-nanoparticle solution was used to fabricate a Cu_2O film.[53,54] However, the formation of a uniform Cu_2O film is difficult due to the agglomeration of nanoparticles in dispersed solution.[51,55] Therefore, both materials and device-fabrication methods should be designed to make an ideal HTL.

Herein, we introduce a one-step deposition of Cu_2O-CuSCN to make an ideal nanocomposite HTL. Cu_2O is initially prepared as a nanoparticle and uniformly dispersed in CuSCN solution in diethylsulfide to simplify the process. Cu_2O at perovskite/CuSCN interface reduced interfacial reaction between perovskite and CuSCN and enhanced the hole-extraction rate, resulting in an improvement of PCE from 17.7% to 19.2% and sustaining 720 h under thermally induced condition (85°C/85% of relative humidity (RH), encapsulated). We have further investigated the distribution of Cu_2O and CuSCN in HTL to confirm the detailed role of nanocomposite. Moreover, electronic and optical behaviors of device and nanocomposite were elucidated to suggest the ideal HTL fabrication in PSCs.

3.2. Experimental Section

Device Fabrication: ITO substrate (AMG) was sonicated in acetone, isopropanol, and deionized water, for 30 min respectively. Then, the substrate was treated by UV-ozone for 15 min. The SnO_2 colloidal dispersion (15 wt. % in H_2O, Alfa Aesar) diluted with DI water was spin coated on ITO glass and annealed at 120°C for 30 min. The substrate for hole-only device was fabricated by spin-coating PTAA solution (2 mg/ml in chlorobenzene) on ITO glass with spin rate of 5000 rpm for 40 s, with annealing at 120°C for 20 min. For the perovskite film, 1.8 M $Cs_{0.05}(FA_{0.85}MA_{0.15})_{0.95}Pb(I_{0.85}Br_{0.15})_3$ precursor was prepared by dissolving formamidinium iodide (Great Solar Laboratory), methylammonium bromide (Great Solar Laboratory), lead iodine (PbI_2: TCI Chemicals), lead bromide ($PbBr_2$: TCI Chemicals), and cesium iodide (Great Solar Laboratory) in *N*,*N*-dimethylformamide (DMF: Sigma-Aldrich) and dimethylsulfoxide (DMSO: Sigma-Aldrich) with 4:1 volume ratio. The perovskite solution was spin-coated on substrate at 5000 rpm for 20 s with 1 mL of diethyl ether (Daejung) used as a secondary solvent. PDMS (Sigma Aldrich) film was prepared by dispersing 12.25 mg of PDMS in 1 mL *n*-Hexane (Daejung) and spin-coated on the perovskite film. For Cu_2O-CuSCN nanocomposite film, 10 mg of Cu_2O (US Research Nanomaterials) and 10 mg of CuSCN (Sigma Aldrich) in 1 mL diethylsulfide (Sigma Aldrich) was spin-coated on substrate with annealing at 50°C for 10 min. For CuSCN film, 25 mg of CuSCN 1 mL diethylsulfide was used for spin-coating with annealing at 50°C for 10 min.

Characterization: Optical properties of various films were analyzed with UV/Vis spectroscopy (V-770: JASCO). An x-ray

diffractometer (New D-8 Advance: Bruker) was used to detect the phases and impurities in perovskite and hole transport materials. A field-emission scanning electron microscope (Merlin Compact: Zeiss) was used to monitor the vertical structures of devices. Raman and steady-state photoluminescence spectra were obtained via LabRAM HV Evolution, Horiba, using lasers of $\lambda_{excitation}$ = 532 nm. Time-resolved PL spectra (FluoTime 300: Picoquant) were obtained using $\lambda_{excitation}$ = 398 nm laser. Time-of-flight secondary-ion mass spectroscopy (TOF.SIMS-5: ION-TOF) was performed to analyze the compositional depth profile of Cu_2O-CuSCN nanocomposite film. Four-point probe was used to measure the electric conductivity of films fabricated on glass substrates. Work functions of argon-sputtered films were measured by multipurpose x-ray photoelectron spectroscopy (Sigma Probe: Thermo VG Scientific) with photon energy of hv = 21.22 eV. A potentiostat (Zive SP-1: WonATech) was utilized for both space-charge-limited current (SCLC) and admittance analyses. For the SCLC measurement, voltage was applied from 0 V to 5 V. For the admittance analysis, the impedance of device was measured under AC voltage perturbation with 10 mV amplitude and frequency from 10^{-2} to 10^5 Hz. The devices had been kept in dark to drop the voltage below 2 mV before each measurement. The solar cell measurement system (K-3000: McScience) was used to test the device performance with an active area of 0.09 cm^2. The voltage was swept from 1.2 to −0.1 V for the reverse scan, or vice versa for the forward scan (scan rate of 100 mV s^{-1}).

3.3. Results and Discussion

Concerning the stability of perovskite photovoltaics, many works were done to investigate the origin of device degradation. There are two main causes of degradation, first is the poor OHP stability, and second is the interfacial reaction between OHP and HTL.[13,29-32,43] Conventional HTL used salt-doped organics, and those were easily degrading and reacting with OHP under operating conditions. Alternatively, CuSCN was introduced as a hole-transport material with high PCE, but the stability problem isn't fully solved, remaining additional room to discover the methods for efficient and stable perovskite solar cells.

Schematics shown in Fig. 3-1(a) illustrates idea of this work. By constructing Cu_2O-CuSCN nanocomposite on top of $Cs_{0.05}(FA_{0.85}MA_{0.15})_{0.95}Pb(I_{0.85}Br_{0.15})_3$ (CsFAMA), the contact area between CuSCN and CsFAMA can be minimized. From the previous reports, OHP and CuSCN makes reaction to produce CuI, which is the main cause of device degradation.[39,42] Therefore, Cu_2O is used to block the interfacial reaction to improve the stability. Moreover, hole mobility of Cu_2O is higher than that of CuSCN, boosting the extraction of holes generated from OHP.[56] We have observed the uniformed film morphology, which is illustrated in Fig. 3-1(b), and the presence of Cu_2O by the XRD diffraction pattern, as shown in Fig. 3-1(c) (XRD of Cu_2O nanoparticle and the optical images of dispersed nanocomposite solution are in Figs. 3-2 and 3-3). Cu_2O solely cannot obtain uniform film, leading to poor device performance as shown in Fig. 3-4. To confirm the chemical distribution of nanocomposite, time-of-flight secondary ion mass spectrometry (ToF-SIMS) was measured. The top layer of HTL contained CuSCN dominantly

while Cu_2O is mainly located below CuSCN. The SiO^- peak was originated by the PDMS interlayer utilized for suppressing interfacial degradation by diethyl sulfide and defect passivation as reported in our previous work.[42] As the Cu_2O location may be a significant key to enhance performance and stability of devices, further analyses are conducted to scrutinize the effects of Cu_2O-CuSCN nanocomposite as a hole-transport layer.

To investigate the charge extraction and electronic structure of Cu2O-CuSCN nanocomposite, optoelectronic properties were investigated. The optical bandgaps were measured for different hole-transport materials, as shown in Fig. 3(a). In the case of nanocomposite material, the bandgap is ~2.2 eV, which deviates from that of Cu2O (~2.1 eV), possibly due to the interfacial disorder or changed bonding nature caused by the coexistence of O and S components. Figs. 3-5(b) and (c) illustrate the electronic structure for individual and nanocomposite materials. As illustrated, work functions and valance-band maxima (VBM) of nanocomposite and CuSCN are quite similar, due to the effective nanometer-scale depth of ultraviolet photoelectron spectroscopy (UPS). On the other hand, Cu2O shows more n-type behavior than CuSCN with higher work function, thereby transporting holes from OHP to CuSCN more efficiently.

The dark current vs. voltage characteristics for hole-only devices are measured to examine the hole mobility of nanocomposite. The $J-V$ curves of device with ITO/PTAA/HTL/Au structure with different HTLs are shown in Fig. 3-5(d), and the charge mobility is 1.53 $cm^2\ V^{-1}\ s^{-1}$ and 0.19 $cm^2\ V^{-1}\ s^{-1}$ for the Cu_2O-CuSCN nanocomposite and CuSCN only devices, respectively.[57] The clear enhancement of the hole mobility was

observed, which will lead to the increase in hole extraction rate and improvement of photovoltaic parameters (4-point probe data is presented in Fig. 3-6). To further scrutinize hole transporting behavior, the photoluminescence (PL) spectroscopy was conducted for glass/CsFAMA/nanocomposite and glass/CsFAMA/CuSCN films as shown in Fig. 3-5(e). The bare CsFAMA film shows high PL intensity with photocarriers dissipating via radiative recombination of electrons and holes. Otherwise, in films with HTL, a large rate of holes is extracted to HTL deriving PL quenching. Conspicuously, for the nanocomposite HTL, more effective PL quenching is detected, indicating that the hole extraction from CsFAMA to HTL is improved. Moreover, as shown in Fig. 3-5(f), time-resolved photoluminescence (TRPL) was further conducted, where the nanocomposite resulted in shorter lifetime than that of CuSCN supporting the improvement of hole-extracting behavior.

The understanding of defect behavior and operation as a device will provide further understanding in this research. Therefore, dark *J-V* curves of ITO/PTAA/CsFAMA/HTL/Au devices are shown in Fig. 3-7(a), and the hole-trap density is evaluated from trap-filled limit voltage (V_{TFL}) which resulted in 1.9×10^{15} cm^{-3} and 4.3×10^{15} cm^{-3} for the Cu_2O-CuSCN nanocomposite device and CuSCN-only device, respectively. The result addresses that the trap sites are apparently reduced by utilizing the nanocomposite.[58] For further analyzation of defects and traps behavior at the perovskite solar cells, the Nyquist plot is determined by electrochemical impedance spectroscopy (EIS) as shown in Fig. 3-7(b). The device with nanocomposite shows a larger semicircle than CuSCN only device, yielding the higher recombination-resisting tendency which reveals

the decrease in trap sites near the interface.[59,60] Additional trap distribution spectra in Fig. 3-7(c) indicate that defects of nanocomposite are shifted by 0.04 eV toward shallower sites. In addition, the lower trap density of the nanocomposite device is observed about than those of the CuSCN-only device.[61-64] As discussed previously, OHP/CuSCN can produce many types of impurities at the interfaces, such as PbI_2 and CuI. Moreover, there are higher possibilities for perovskite to obtain more defects than CuSCN layer, because the halide migration occurs frequently during the operating conditions (light, heat, and air). Therefore, Cu_2O suppresses the formation of defects at the interface between CsFAMA and CuSCN, improving the charge transport and decreasing defect concentration resulting in reduced carrier recombination at the interface (Fig. 3-7(d)).

Due to the fast charge extraction and depressed defects by utilizing the nanocomposite HTL, power conversion efficiency (PCE) is largely improved from 17.7% to 19.2% (Fig. 3-8(a), optimization processes are in Figs. 3-9 and 3-10). Steady-state current is further conducted in Fig. 3-8(b), and devices with nanocomposite achieve saturation point faster than devices with CuSCN only. These observations address that photo-generated charges are properly transporting to build up circuit without traps, allowing largely lowered hysteresis as shown in Fig. 3-8(c). Depending on the direction of a voltage bias, charge trap can occur by distortion of bands, but the presence of Cu_2O possibly hinders the distortion of bands, resulting in low hysteresis. In Fig. 3-8(d), EQE is conducted to further confirm the tendency of current generation. Even though the possible additional absorption by the bandgap of Cu2O-CuSCN HTL (~550 nm)[65] is almost nonexistent in the EQE spectra, probably due to the n-i-p sequential

structure, the improved hole extraction behavior of nanocomposite HTL may contribute to the EQE improvement at approximately 700-nm range, which results in an increase of net current for the device adopting nanocomposite HTL.

One of the critical issues in perovskite research is degradation reaction that hampers the long-term stability, occurring both in CsFAMA and interface between CsFAMA and HTL. Nanocomposite HTL reduced trap density, lowering the degradation sites of material. Moreover, the interfacial reaction of CsFAMA and CuSCN can be reduced during the operating condition. Therefore, as stored under the heat and humidity induced condition (85°C/85% RH, encapsulated), the thermal stability is largely improved from 480 h to 720 h by using nanocomposite as an HTL, sustaining over 90% of its initial PCE as shown in Fig. 3-11(a) (additional thermal stabilities and *J-V* parameters are shown in Fig. 3-12). To understand the mechanism in more detail, devices were stored under 85°C/85% RH condition for 720 h with encapsulation and observed the degradation by XRD. As shown in Fig. 3-11 (b), PbI_2 and CuI were dominantly formed at the bare CuSCN device compared to the nanocomposite device. Formation of PbI_2 is the main critical issue of CsFAMA, and nanocomposite-based device formed less PbI_2 than bare device because of the lower defect density. More importantly, the absence of CuI, the clear evidence of interfacial reaction, indicates that nanocomposite HTL perfectly suppressed the device degradation occuring at the CsFAMA/CuSCN interface.

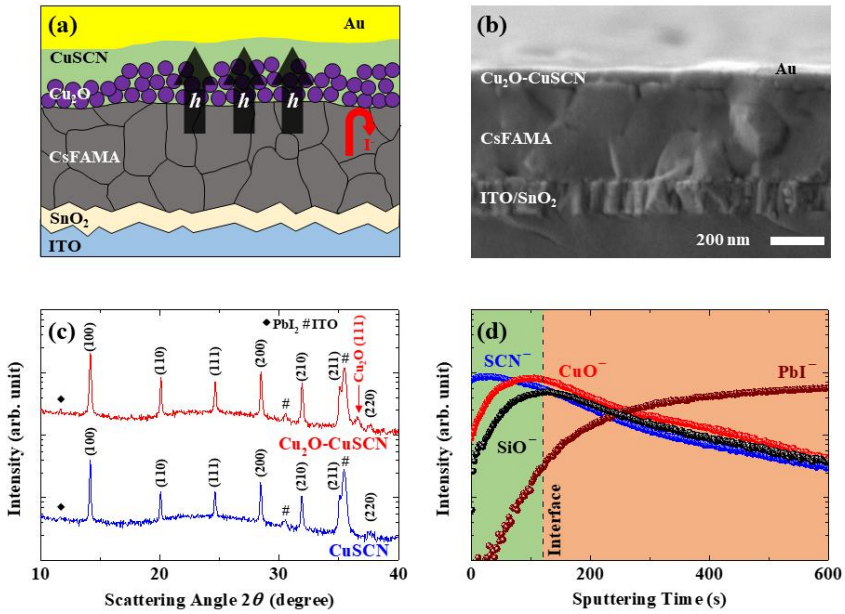

Fig. 3-1. (Color) Schematics and characterization of the Cu_2O-CuSCN nanocomposite layer. (a) The device architecture and (b) cross-sectional SEM image of the Cu_2O-CuSCN based device. (c) XRD patterns with different HTLs deposited on the $Cs_{0.05}(FA_{0.85}MA_{0.15})_{0.95}Pb(I_{0.85}Br_{0.15})_3$ (CsFAMA) films. (d) ToF-SIMS depth profile of the ITO/SnO_2/CsFAMA/Cu_2O-CuSCN film. The SiO^- is originated by the PDMS interlayer at the CsFAMA/HTL interface.

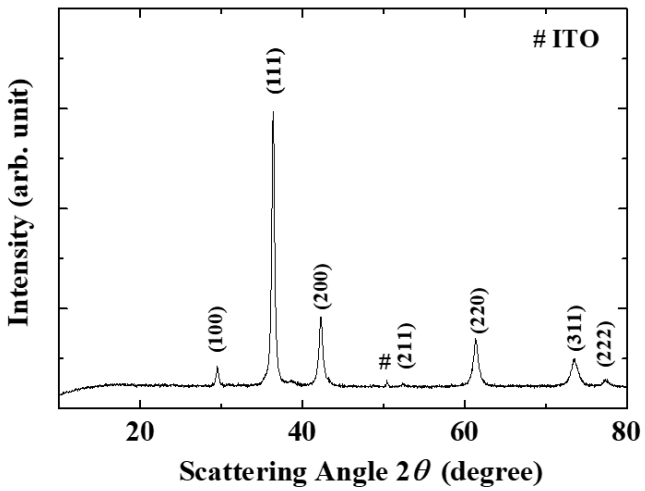

Fig. 3-2. (Color) X-ray diffraction pattern of the Cu_2O nanoparticles.

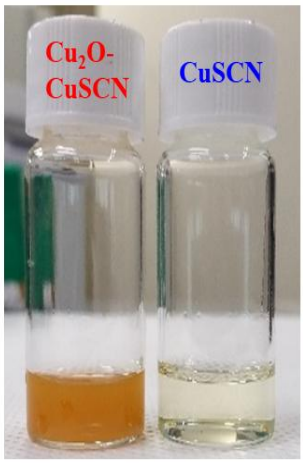

Fig. 3-3. (Color) Optical images of the Cu_2O-CuSCN and CuSCN solutions in diethylsulfide.

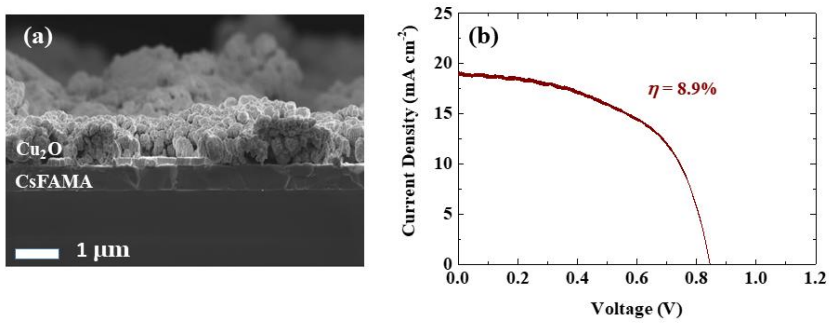

Fig. 3-4. (Color) Cross-sectional SEM image and *J-V* plot of the device utilizing Cu_2O as a HTL.

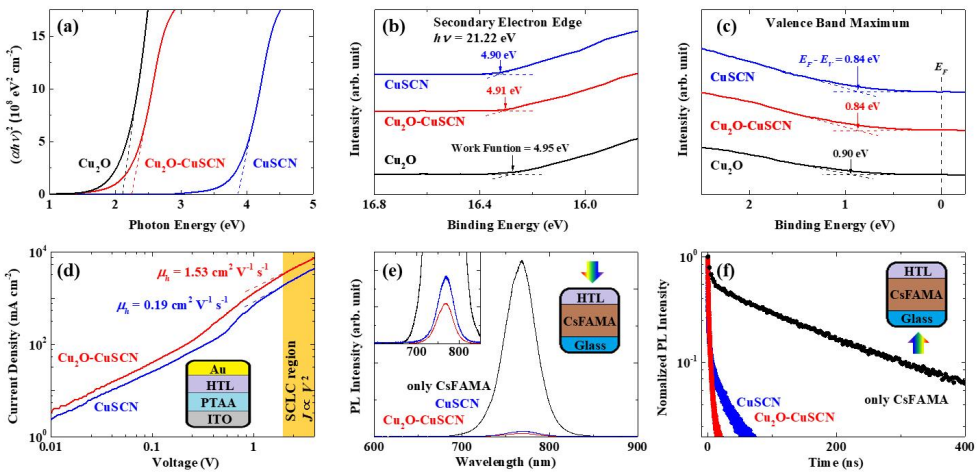

Fig. 3-5. (Color) Optical and electronic properties of Cu_2O-CuSCN nanocomposite HTL. (a) Bandgap energy of each HTL. (b) Work function from the secondary electron edge, and (c) valence band maximum for each HTL deposited on the ITO/SnO_2/CsFAMA film. (d) *J-V* characteristics of hole-only devices with fitted lines in the space-charge limited current (SCLC) region. (e) Steady-state photoluminescence (PL) spectra with a magnified image in the inset, and (f) time-resolved PL of various films deposited on glass substrates.

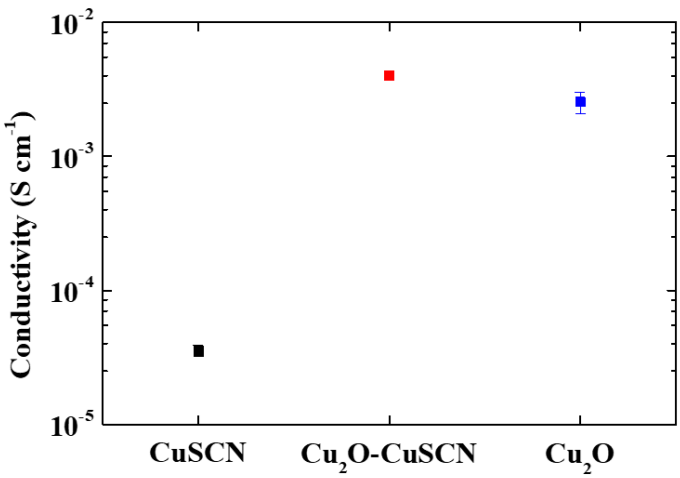

Fig. 3-6. (Color) Electrical properties of various HTLs. In-plane conductivity is measured by four-point probe for CuSCN, Cu_2O-CuSCN nanocomposite, and Cu_2O films deposited on glass substrates.

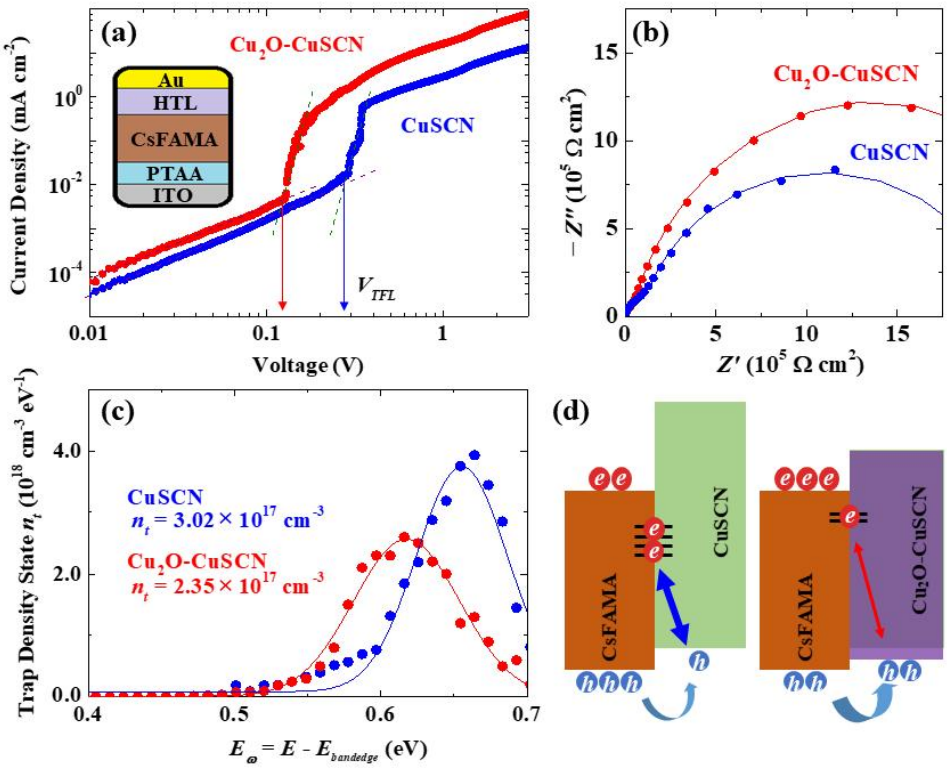

Fig. 3-7. (Color) Trap density analyses and energy level diagram of the devices with different HTLs. (a) *J-V* characteristics of hole-only devices with perovskite layer, with arrows marking the trap-filled limited voltage (V_{TFL}). (b) Nyquist plots and (c) trap distribution spectra from the capacitance-frequency analyses. (d) Schematics of the band structure and trap states at the CsFAMA/HTL interface of each device.

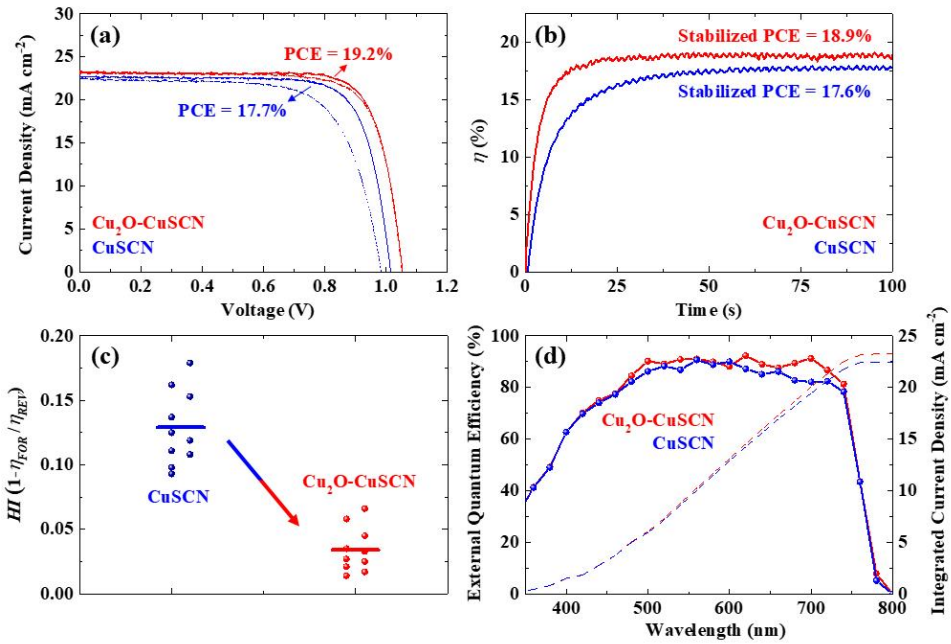

Fig. 3-8. (Color) Enhancement of the perovskite solar cells by utilizing Cu_2O-CuSCN HTLs. (a) *J-V* characteristics, (b) steady-state efficiency under the maximum power voltage, (c) hysteresis index ($HI = 1-\eta_{FOR}/\eta_{REV}$), and (d) external quantum efficiency of the perovskite solar cells.

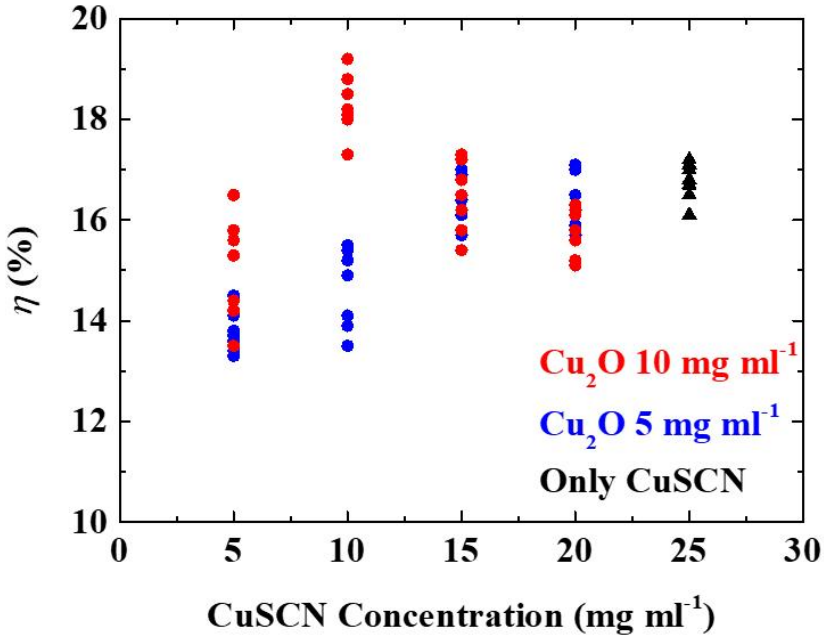

Fig. 3-9. (Color) Optimization of the Cu_2O and CuSCN concentrations of nanocomposite based devices. Comparison of the performances for 7 devices at each condition. The optimum condition is 10 mg/ml for both Cu_2O and CuSCN.

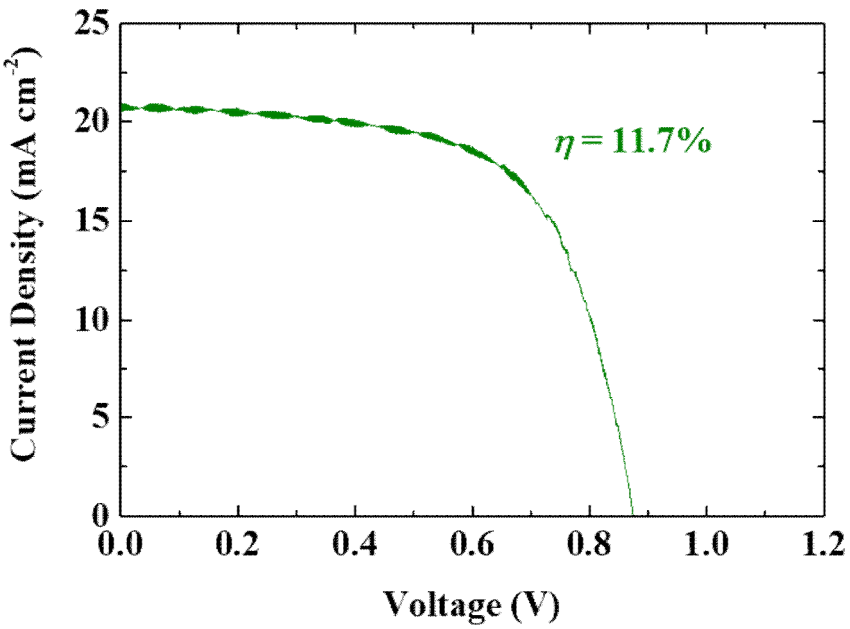

Fig. 3-10. (Color) The *J-V* plot of the device with a bilayer-deposited HTL**.** The perovskite solar cells were fabricated by the following sequence: 10 mg/ml of Cu_2O-dispersion solution was spin coated on a perovskite film, then 10 mg/ml of CuSCN solution was deposited subsequently.

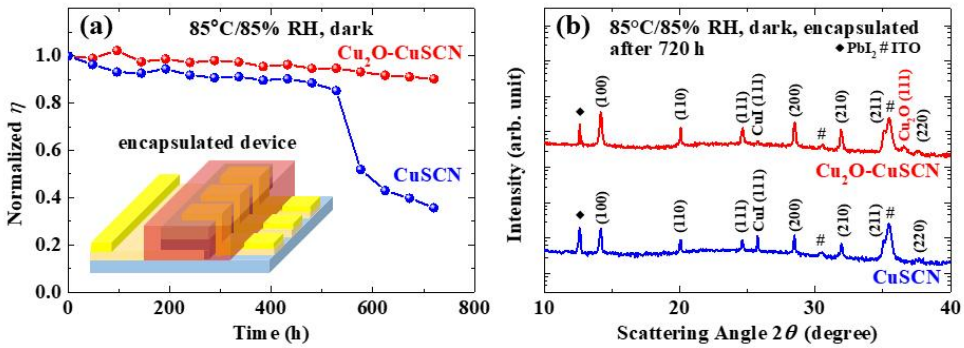

Fig. 3-11. (Color) Long-term stability of the solar cells with different HTLs. (a) Thermal stability of the devices, and (b) XRD of the devices stored under 85°C/85% RH for 720 h (with gold removed before the diffraction measurements).

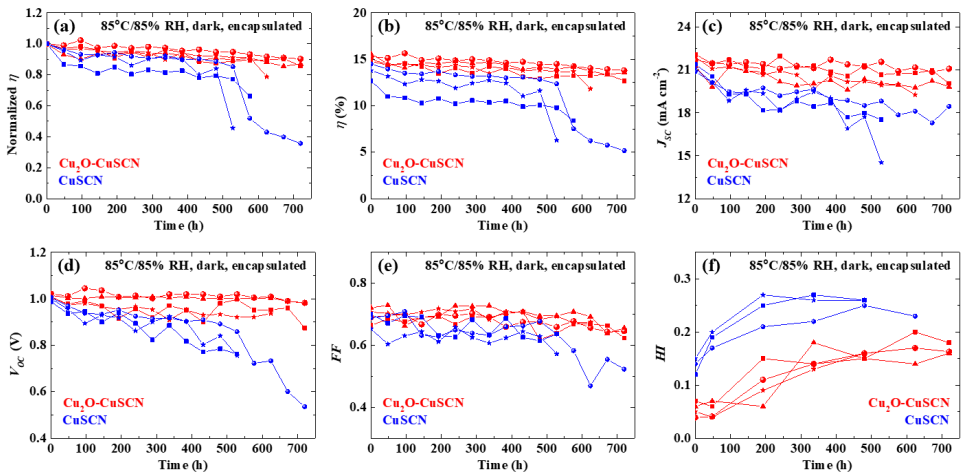

Fig. 3-12. (Color) Long-term stability for several devices with different HTLs. (a) Normalized η, (b) η, (c) J_{SC}, (d) V_{OC}, (e) FF, and (h) HI of the devices stored under 85°C/85% RH with encapsulation in dark condition.

3.4. Conclusions

Conventional organic HTLs for perovskite solar cells have issues of low material stability and interfacial reaction with OHP, requiring alternative HTL. CuSCN HTL was widely studied as alternatives, yet interfacial reaction remained as main bottleneck in this field. Cu_2O-CuSCN nanocomposite is utilized as ideal HTL, exhibiting both high PCE and high stability under extreme conditions. Cu_2O in nanocomposite shows faster extraction of charges that were generated in OHP, and it also suppresses the interaction between OHP and CuSCN to minimize the interfacial reaction. The novel design of nanocomposite and facile process may enable the fields of HTL and perovskite to get closer to the commercialization.

3.5. References

[1] Shin, B.; Zhu, Y.; Gunawan, O.; Bojarczuk, N. A.; Chey, S. J.; Guha, S. Thin Film Solar Cell with 8.4% Power Conversion Efficiency Using an Earth-Abundant Cu_2ZnSnS_4 Absorber. *Prog. Photovolt: Res. Appl.* **2013**, *21*, 72-76.

[2] Lee, S.; Flanagan, J. C.; Lee, B.; Hwang, T. ; Kim, J.; Gil, B.; Shim, M.; Park, B. Route to Improving Photovoltaics Based on CdSe/$CdSe_xTe_{1-x}$ Type-II Heterojunction Nanorods: The Effect of Morphology and Cosensitization on Carrier Recombination and Transport. *ACS Appl. Mater. Interfaces* **2017**, *9*, 31931- 31939.

[3] Park, H. H.; Heasley, R.; Sun, L.; Steinmann, V.; Jaramillo, R.; Hartman, K.; Chakraborty, R.; Sinsermsuksakul, P.; Chua, D.; Buonassisi, T.; Gordon, R. G. Co-Optimization of SnS Absorber and Zn (O, S) Buffer Materials for Improved Solar Cells. *Prog. Photovolt: Res. Appl*. **2015**, *23*, 901-908.

[4] Saive, R.; Boccard, M.; Saenz, T.; Yalamanchili, S.; Bukowsky, C. R.; Jahelka, P.; Yu, Z. J.; Shi, J.; Holmanb, Z.; Atwater, H. A. Silicon Heterojunction Solar Cells with Effectively Transparent Front Contacts. *Sustainable Energy Fuels* **2017**, *1*, 593.\

[5] Lee, S.; Flanagan, J. C.; Kim, J.; Yun, A. J.; Lee, B.; Shim, M.; Park, B. Efficient Type-II Heterojunction Nanorod Sensitized Solar Cells Realized by Controlled Synthesis of Core/Patchy-Shell Structure and CdS Cosensitization. *ACS Appl. Mater. Interfaces* **2019**, *11*, 19104-19114.

[6] Snaith, H. J. Perovskites: The Emergence of a New Era for Low-Cost, High-Efficiency Solar Cells. *J. Phys. Chem. Lett*. **2013**, *4*, 3623-3630.

[7] Frost, J. M.; Butler, K. T.; Brivio, F.; Hendon, C. H.; Schilfgaarde, M. V.; Walsh, A. Atomistic Origins of High-Performance in Hybrid Halide Perovskite Solar Cells. *Nano Lett*. **2014**, *14*, 2584-2590.

[8] Song, Z.; Watthage, S. C.; Phillips, A. B.; Liyanage, G. K.; Khanal, R. R.; Tompkins, B. L.; Ellingson, R. J.; Heben, M. J. Investigation of Degradation Mechanisms of Perovskite-Based Photovoltaic Devices Using Laser Beam Induced Current Mapping. *Proc. of SPIE* **2015**, *9561*, 956107.

[9] Lee, B.; Lee, S.; Cho, D.; Kim, J.; Hwang, T.; Kim, K. H.; Hong, S.; Moon, T.; Park, B. Evaluating the Optoelectronic Quality of Hybrid Perovskites by Conductive Atomic Force Microscopy with Noise Spectroscopy. *ACS Appl. Mater. Interfaces* **2016**, *8*, 30985-30991.

[10] Hodes, G. Perovskite-Based Solar Cells. *Science* **2013**, *342*, 317-318.

[11] Lian, J.; Lu, B.; Niu, F.; Zeng, P.; Zhan, X. Electron-Transport Materials in Perovskite Solar Cells. *Small Methods* **2018**, *2*, 1800082.

[12] Kim, J.; Hwang, T.; Lee, S.; Lee, B.; Kim, J.; Kim, J.; Gil, B.; Park, B. Synergetic Effect of Double-Step Blocking Layer for the Perovskite Solar Cell. *J. Appl. Phys*. **2017**, *122*, 145106.

[13] Li, N.; Tao, S.; Chen, Y.; Niu, X.; Onwudinanti, C. K.; Hu, C.; Qiu, Z.; Xu, Z.; Zheng, G.; Wang, L.; Zhang, Y.; Li, L.; Liu, H.; Lun, Y.; Hong, J.; Wang, X.; Liu, Y.; Xie, H.; Gao, Y.; Bai, Y.; Yang, S.; Brocks, G.; Chen, Q.; Zhou, H. Cation and Anion Immobilization Through Chemical Bonding Enhancement with Fluorides for Stable Halide Perovskite Solar Cells. *Nat. Energy* **2019**, *4*, 408.

[14] Hwang, T.; Lee, B.; Kim, J.; Lee, S.; Gil, B.; Yun, A. J.; Park, B. From Nanostructural Evolution to Dynamic Interplay of Constituents: Perspectives for Perovskite Solar Cells. *Adv. Mater*. **2018**, *30*, 1704208.

[15] Kojima, A.; Teshima, K.; Shirai, Y.; Miyasaka, T. Organometal Halide Perovskites as Visible-Light Sensitizers for Photovoltaic Cells. *J. Am. Chem. Soc*. **2009**, *131*, 6050-6051.

[16] Todorov, T.; Gershon, T.; Gunawan, O.; Lee, Y. S.; Sturdevant, C.; Chang. L. Y.; Guha, S.; Monolithic Perovskite-CIGS Tandem Solar

Cells via In Situ Band Gap Engineering. *Adv. Energy Mater.* **2015**, *5*, 1500799.

[17] Kim, J.; Hwang, T.; Lee, S.; Lee, B.; Kim, J.; Jang, G. S.; Nam, S.; Park, B. Solvent and Intermediate Phase as Boosters for the Perovskite Transformation and Solar Cell Performance. *Sci. Rep*. **2016**, *6*, 25648.

[18] Kim, J.; Yun, A. J.; Gil, B.; Lee, Y.; Park, B. Triamine-Based Aromatic Cation as a Novel Stabilizer for Efficient Perovskite Solar Cells. *Adv. Funct. Mater.* **2019**, *29*, 1905190.

[19] NREL, Best Research-Cell Efficiency Chart. https://www.nrel.gov/pv/cell-efficiency.html (accessed November 6 2019).

[20] Kim, D.; Kim, G. Y.; Ko, C.; Pae, S. R.; Lee, Y. S.; Gunawan, O.; Ogletree, D. F.; Jo, W.; Shin, B. Effects of Postsynthesis Thermal Conditions on Methylammonium Lead Halide Perovskite: Band Bending at Grain Boundaries and Its Impacts on Solar Cell Performance. *J. Phys. Chem. C* **2016**, *120*, 21330-21335.

[21] Hwang, T.; Lee, S.; Kim, J.; Kim, J.; Kim, C.; Shin, B.; Park, B. Tailoring the Mesoscopic TiO_2 Layer: Concomitant Parameters for Enabling High-Performance Perovskite Solar Cells. *Nanoscale Res. Lett.* **2017**, *12*, 57.

[22] Wieghold, S.; Correa-Baena, J.-P.; Nienhaus, L.; Sun, S.; Shulenberger, K. E.; Liu, Z.; Tresback, J. S.; Shin, S. S.; Bawendi, M. G.; Buonassisi, T. Precursor Concentration Affects Grain Size, Crystal Orientation, and Local Performance in Mixed-Ion Lead Perovskite Solar Cells. *ACS Appl. Energy Mater.* **2018**, *1*, 6801-6808.

[23] Lee, B.; Shin, B.; Park, B. Uniform Cs_2SnI_6 Thin Films for Lead-Free and Stable Perovskite Optoelectronics via Hybrid Deposition Approaches. *Electron. Mater. Lett.* **2019**, *15*, 192-200.

[24] Jung, H. J.; Kim, D.; Kim, S.; Park, J.; Dravid, V. P.; Shin, B. Stability of Halide Perovskite Solar Cell Devices: In Situ Observation of Oxygen Diffusion under Biasing. *Adv. Mater.* **2018**, *30*, 1802769.

[25] Kim, J.; Hwang, T.; Lee, B.; Lee, S.; Park, K.; Park, H. H.; Park, B. An Aromatic Diamine Molecule as the A-Site Solute for Highly Durable and Efficient Perovskite Solar Cells. *Small Methods* **2019**, *3*, 1800361.

[26] Lee, B.; Hwang, T.; Lee, S.; Shin, B.; Park, B. Microstructural Evolution of Hybrid Perovskites Promoted by Chlorine and its Impact on the Performance of Solar Cell. *Sci. Rep*. **2019**, *9*, 4803.

[27] Zhang, H.; Shi, Y.; Yan, F.; Wang, L.; Wang, K.; Xing, Y.; Dong, Q.; Ma, T. A Dual Functional Additive for the HTM Layer in Perovskite Solar Cells. *Chem. Commun.* **2014**, *50*, 5020-5022.

[28] Leijtens, T.; Bush, K.; Cheacharoen, R.; Beal, R.; Bowring, A.; McGehee, M. D. Towards Enabling Stable Lead Halide Perovskite Solar Cells; Interplay Between Structural, Environmental, and Thermal stability. *J. Mater. Chem. A* **2017**, *5*, 11483.

[29] Liu, Q.; Fan, L.; Zhang, Q.; Zhou, A.; Wang, B.; Bai, H.; Tian, Q.; Fan, B.; Zhang, T. Benzoyl Peroxide as an Efficient Dopant for Spiro-OMeTAD in Perovskite Solar Cells. *ChemSusChem* **2017**, *10*, 3098-3104.

[30] Jena, A. K.; Numata, Y.; Ikegami, M.; Miyasaka, T. Role of Spiro-OMeTAD in Performance Deterioration of Perovskite Solar Cells at High Temperature and Reuse of the Perovskite Films to Avoid Pb-Waste. *J. Mater. Chem. A* **2018**, *6*, 2219.

[31] Gu, X.; Li, Y.; Mu, Y.; Zhang, M.; Lu, T.; Wang, P. $FeCl_3$ as a Low-Cost and Efficient *p*-Type Dopant of Spiro-OMeTAD for High Performance Perovskite Solar Cells. *RSC Adv.* **2018**, *8*, 9409-9413.

[32] Gratia, P.; Magomedov, A.; Malinauskas, T.; Daskeviciene, M.; Abate, A.; Ahmad, S.; Grätzel, M.; Getautis, V.; Nazeeruddin, M. K. A Methoxydiphenylamine-Substituted Carbazole Twin Derivative: An Efficient Hole-Transporting Material for Perovskite Solar Cells. *Angew. Chem., Int. Ed*. **2015**, *54*, 11409-11413.

[33] Jung, M.; Kim, Y. C.; Jeon, N. J.; Yang, W. S.; Seo, J.; Noh, J. H.; Seok, S. I. Thermal Stability of CuSCN Hole Conductor-Based Perovskite Solar Cells. *ChemSusChem* **2016**, *9*, 2592-2596.

[34] Wu, Q.; Xue, C.; Li, Y.; Zhou, P.; Liu, W.; Zhu, J.; Dai, S.; Zhu, C.; Yang, S. Kesterite Cu_2ZnSnS_4 as a Low-Cost Inorganic Hole-Transporting Material for High-Efficiency Perovskite Solar Cells. *ACS Appl. Mater. Interfaces* **2015**, *7*, 28466.

[35] Cao, J.; Yu, H.; Zhou, S.; Qin, M.; Lau, T.-K.; Lu, X.; Zhao, N.; Wong, C.-P. Low-Temperature Solution-Processed NiO_x Films for Air-Stable Perovskite Solar Cells. *J. Mater. Chem. A* **2017**, *5*, 11071-11077.

[36] Arora, N.; Dar, M. I.; Hinderhofer, A.; Pellet, N.; Schreiber, F.; Zakeeruddin, S. M.; Grätzel, M. Perovskite Solar Cells with CuSCN

Hole Extraction Layers Yield Stabilized Efficiencies Greater than 20%. *Science* **2017**, *358*, 768-771.

[37] Gil, B.; Yun, A. J.; Lee, Y.; Kim, J.; Lee, B.; Park, B. Recent Progress in Inorganic Hole Transport Materials for Efficient and Stable Perovskite Solar Cells *Electron. Mater. Lett.* **2019**, *15*, 505-524.

[38] Yang, I. S.; Sohn, M. R.; Sung, S. D.; Kim, Y. J.; Yoo, Y. J.; Kim, J. H.; Lee, W. I. Formation of Pristine CuSCN Layer by Spray Deposition Method for Efficient Perovskite Solar Cell with Extended Stability. *Nano Energy* **2017**, *32*, 414-421.

[39] Liu, J.; Pathak, S. K.; Sakai, N.; Sheng, R.; Bai, S.; Wang, Z.; Snaith, H. J. Identification and Mitigation of a Critical Interfacial Instability in Perovskite Solar Cells Employing Copper Thiocyanate Hole-Transporter. *Adv. Mater. Interfaces* **2016**, *3*, 1600571.

[40] Madhavan, V. E.; Zimmermann, I.; Roldan-Carmona, C.; Grancini, G.; Buffiere, M.; Belaidi, A.; Nazeeruddin, M. K. Copper Thiocyanate Inorganic Hole-Transporting Material for High-Efficiency Perovskite Solar Cells. *ACS Energy Lett.* **2016**, *1*, 1112-1117.

[41] Yu, W.; Li, F.; Wang, H.; Alarousu, E.; Chen, Y.; Lin, B.; Wang, L.; Hedhili, M. N.; Li, Y.; Wu, K.; Wang, X.; Mohammedc, O. F.; Wu, T. Ultrathin Cu_2O as an Efficient Inorganic Hole Transporting Material for Perovskite Solar Cells. *Nanoscale* **2016**, *8*, 6173-6179.

[42] Kim, J.; Lee, Y.; Yun, A. J.; Gil, B.; Park, B. Interfacial Modification and Defect Passivation by Crosslinking Interlayer for Efficient and Stable CuSCN-Based Perovskite Solar Cell. ACS Appl. Mater. Interfaces **2019**.

[43] Mali, S. S.; Patil, J. V.; Kim, H.; Luque, R.; Hong, C. K. Highly Efficient Thermally Stable Perovskite Solar Cells via Cs:NiO_x/CuSCN Double-Inorganic Hole Extraction Layer Interface Engineering. *Materials today* **2019**, *26*, 8-18.

[44] Guo, Y.; Lei, H.; Xiong, L.; Li, B.; Chen, Z.; Wen, J.; Yang, G.; Li, G.; Fang, G. Single Phase, High Hole Mobility Cu_2O Films as an Efficient and Robust Hole Transporting Layer for Organic Solar Cells. J. Mater. Chem. A **2017**, *5*, 11055-11062.

[45] Wilson, S. S.; Bosco, J. P.; Tolstova, Y.; Scanlon, D. O.; Watson, G. W.; Atwater, H. A. Interface Stoichiometry Control to Improve Device Voltage and Modify Band Alignment in ZnO/Cu_2O Heterojunction Solar Cells. *Energy Environ. Sci.* **2014**, *7*, 3606.

[46] Lien, H. T.; Wong, D. P.; Tsao, N. H.; Huang, C. I.; Su, C.; Chen, K. H.; Chen, L. C. Effect of Copper Oxide Oxidation State on The Polymer-Based Solar Cell Buffer Layers. *ACS Appl. Mater. Interfaces* **2014**, *6*, 22445.

[47] Lin, L.; Jiang, L.; Li, P.; Fan, B.; Qui, Y. A Modeled Perovskite Solar Cell Structure with a Cu_2O Hole-Transporting Layer Enabling over 20% Efficiency by Low-Cost Low-Temperature Processing. *Journal of Physics and Chemistry of Solids* **2019**, *124*, 205-211.

[48] Chatterjee, S.; Pal, A. J. Introducing Cu_2O Thin Films as a Hole-Transport Layer in Efficient Planar Perovskite Solar Cell Structures. *J. Phys. Chem. C* **2016**, *120*, 1428-1437.

[49] Liu, L.; Xi, Q.; Gao, G.; Yang, W.; Zhou, H.; Zhao, Y.; Wu, C.; Wang, L.; Xu, J. Cu_2O Particles Mediated Growth of Perovskite for High

Efficient Hole-Transporting-Layer free Solar Cells in Ambient Condition. *Solar Energy Materials and Solar Cells* **2016**, *157*, 937-942.

[50] Liu, C.; Zhou, X.; Chen, S.; Zhao, X.; Dai, S.; Xu, B. Hydrophobic Cu_2O Quantum Dots Enabled by Surfactant Modification as Top Hole-Transport Materials for Efficient Perovskite Solar Cells. *Adv. Sci.* **2019**, *6*, 1801169.

[51] Zuo, C.; Ding, L. Solution-Processed Cu_2O and CuO as Hole Transport Materials for Efficient Perovskite Solar Cells. *Small* **2015**, *11*, 5528-5532.

[52] Elseman, A. M.; Selim, M. S.; Luo, L.; Xu, C. Y.; Wang, G.; Jiang, Y.; Liu, D. B.; Hao, Z.; Song, Q. L. Efficient and Stable Planar n-i-p Perovskite Solar Cells with Negligible Hysteresis through Solution-Processed Cu_2O Nanocubes as a Low-Cost Hole-Transport Material. *Chemsuschem* **2019**, *12*, 3808-3816.

[53] Liu, C.; Zhou, X.; Chen, S.; Zhao, X.; Dai, S.; Xu, B. Hydrophobic Cu_2O Quantum Dots Enabled by Surfactant Modification as Top Hole-Transport Materials for Efficient Perovskite Solar Cells. *Advanced Science* **2019**, *6*, 1801169.

[54] Lee, B.; Yun, A. J.; Kim, J.; Gil, B.; Shin, B.; Park, B. Aminosilane-Modified $CuGaO_2$ Nanoparticles Incorporated with CuSCN as a Hole-Transport Layer for Efficient and Stable Perovskite Solar Cells. *Adv. Mater. Interfaces* **2019**, *6*, 1901372.

[55] Musa, A. O.; Akomolafe, T.; Carter, M. J. Production of Cuprous Oxide, a Solar Cell Material, by Thermal Oxidation and a Study of Its

Physical and Electrical Properties. *Solar Energy Materials and Solar Cells* **1998**, *51*, 305-316.

[56] Kim, Y.; Jung, E. H., Kim, G.; Kim, D.; Kim, B. J.; Seo. J. Sequentially Fluorinated PTAA Polymers for Enhancing V_{OC} of High-Performance Perovskite Solar Cells. *Adv. Energy Mater*. **2018**, *8*, 1801668.

[57] Bube, R. H. Trap Density Determination by Space-Charge-Limited Currents. *J. Appl. Phys.* **1962**, *33*, 1733–1737.

[58] Guerrero, A.; Garcia-Belmonte, G.; Mora-Sero, I.; Bisquert, J.; Kang, Y. S.; Jacobsson, T. J.; Correa-Baena, J.-P.; Hagfeldt, A. Properties of Contact and Bulk Impedances in Hybrid Lead Halide Perovskite Solar Cells Including Inductive Loop Elements. *J. Phys. Chem. C* **2016**, *120*, 8023-8032.

[59] Tu, Y.; Wu, J.; Zheng, M.; Hua, J.; Pei, Z.; Zhang, L.; Lin, J.; Huang, M. TiO_2 Quantum Dots as Superb Compact Block Layer for High-Performance $CH_3NH_3PbI_3$ Perovskite Solar Cells with Efficiency of 16.97%. Nanoscale **2015**, *7*, 20539-20546.

[60] Hwang, T.; Yun, A. J.; Kim, J.; Cho, D.; Kim, S.; Hong, S.; Park, B. Electronic Traps and Their Correlations to Perovskite Solar Cell Performance via Compositional and Thermal Annealing Controls. *ACS Appl. Mater. Interfaces* **2019**, *11*, 6907-6917.

[61] Yun, A. J.; Kim, J.; Hwang, T.; Park, B. Origins of Efficient Perovskite Solar Cells with Low-Temperature Processed SnO_2 Electron Transport Layer. *ACS Appl. Energy Mater.* **2019**, *2*, 3554-3560.

[62] Hwang, T.; Yun, A. J.; Lee, B.; Kim, J.; Lee, Y.; Park, B. Methylammonium-Chloride Post-Treatment on Perovskite Surface and Its Correlation to Photovoltaic Performance in the Aspect of Electronic Traps. *J. Appl. Phys*. **2019**, *126*, 023101.

[63] Prochowicz, D.; Yadav, P.; Saliba, M.; Saski, M.; Zakeeruddin, S. M.; Lewinski, J.; Grätzel, M. Reduction in the Interfacial Trap Density of Mechanochemically Synthesized $MAPbI_3$. *ACS Appl. Mater. Interfaces* **2017**, *9*, 28418-28425.Lien, H. T.; Wong, D. P.; Tsao, N. H.; Huang, C. I.; Su, C.; Chen, K. H.; Chen, L. C. Effect of Copper Oxide Oxidation State on The Polymer-Based Solar Cell Buffer Layers. *ACS Appl. Mater. Interfaces* **2014**, *6*, 22445.

[64] Lin, C. T.; Rossi, F. D.; Kim, J.; Baker, J.; Ngiam, J.; Xu, B.; Pont, S.; Aristidou, N.; Haque, S. A.; Watson, T.; McLachlan, M. A.; Durrant, J. R. Evidence for Surface Defect Passivation as The Origin of The Remarkable Photostability of Unencapsulated Perovskite Solar Cells Employing Aminovaleric Acid as a Processing Additive. *J. Mater. Chem. A* **2019**, *7*, 3006-3011.

Abstract

유기/무기 하이브리드 페로브스카이트 태양전지 (PSC)는 탁월한 성능을 가진 가장 유망한 태양전지 중 하나입니다. 그러나, 일반적으로 사용되는 유기 정공 수송 재료는 결함 확산 및 흡습성 특성 때문에 열, 광 및 외부 전압이 존재하는 상황에서의 열화를 겪습니다. 이전의 HTM에서 이러한 문제를 해결하기 위해, 화학적 안정성이 우수하고, 캐리어 이동성이 높으며, 비용이 저렴한 무기 재료가 사용되어 고온 및 빛과 같은 조건 하에서 안정성이 향상되었습니다. 보다 안정적이고 효율적인 PSC를 실현하기 위해서는 대체 무기 HTM의 특성을 이해하는 것이 중요합니다. 페로브스카이트 태양전지에서 무기 정공 수송층에 대한 연구는 염 도핑제를 갖는 유기 정공 수송층이 주로 분해 메커니즘에 참여하여 PSC의 효율과 안정성을 저하시킨다는 단점으로 인해 주목을 받고 있습니다. 그러나, 무기질 정공 수송층은 보다 우수한 안정성을 보장하는 한편, 증착 및 계면 제어에 어려움을 가지기 때문에 고성능 태양전지 개발에 큰 어려움이 존재합니다. 또한, 유기 정공 수송층의 분해에 의한 효율 저하를 방지하기 위해 무기계 CuSCN HTL이 대안으로 등장했지만 계면 반응성은 명확하게 밝혀지지 않았습니다.

폴리디메틸실록산(PDMS)은 계면 분해를 방지하고 그의 가교 거동에 의해 CuSCN 기반 PSC의 효율 및 안정성 모두를 향상시키는 이상적인 중합체 중간층 역할을 한다는 점이 입증되었습니다. 놀랍게도, PDMS 중합체는 라만 분광법에 의해 나타낸 바와 같이 페로브스카이트 및 CuSCN과 화학적 결합을 형성하는 것으로 확인되었습니다. PDMS을 활용한 새로운 가교 중간층은 계면에서의 정공 수송 특성을 향상시키고 계면 결함을 낮추어, 19% 이상의 높은 전력 변환 효율을 보였습니다. 또한, PDMS 중간층의 이용은 계면 결함 및 상호 확산을 완화함으로써 습도 및 열 상황에 대한 태양전지의 안정성을 크게 개선시켰습니다. PDMS를 활용한 PSC는 encapsulation이 되지 않은 상태에서 공기 노출 상황에서 1000 시간, 그리고 encapsulation이 된 상태에서 85° C /

85% 상대 습도 조건에서 500 시간 후에도 초기 효율의 90% 이상을 유지했습니다.

Cu_2O와 CuSCN은 효율적이고 안정적인 정공 수송층으로 함께 활용되었습니다. Cu_2O는 가장 높은 정공 이동도를 갖는 물질로 알려져 있지만, 균일한 필름의 형성은 용매의 선택의 제한 및 필름 형성의 불량으로 인해 큰 어려움으로 남아 있습니다. 따라서, Cu_2O-CuSCN 나노 복합체는 우수한 HTL로 제조되었으며, 19.2%의 전력 변환 효율(PCE)을 나타내고 극한 조건 (85℃ / 85%의 상대 습도, encapsulated)에서 720 시간 동안 초기 효율의 90% 이상을 유지하였습니다. 나노 복합체 HTM의 분포는 2차 이온 분광법 (SIMS)에 의해 분석되었으며, XRD를 통해 Cu_2O가 페로브스카이트와 CuSCN 사이의 계면을 명확하게 보호하고 있음을 확인하였습니다. 또한, Cu_2O의 우수한 정공 수송 특성은 전하 추출 속도를 개선하고 재조합을 감소시켰으며, 이는 광발광 (PL) 및 전기 화학 임피던스 분광법 (EIS)에 의해 수행되었습니다.